Insulator – half metallic transition by the tetragonal distortion: A first – principles study of strain – induced perovskite $RbMnF_3$

Namsrai Tsogbadrakh[1],* N. Tuvjargal[1], Chun Feng[1,2], J. Davaasambuu[1], and O. Tegus[2]

[1]*Department of Physics, Natural Science Division, School of Arts and Sciences, National University of Mongolia, Ulaanbaatar 14201, Mongolia*

[2]*Inner Mongolia Key Laboratory for Physics and Chemistry of Functional Materials, Inner Mongolia Normal University, Hohhot 010022, China*

From the spin polarized density functional total energy calculations, we shown that the ground state of cubic perovskite $RbMnF_3$ is an antiferromagnetic (AFM) insulator due to the super – exchange mechanism, in agreement with the other theoretical and experimental results. After tetragonal distortion along the c – axis, keeping the predicted volume, our results indicated that the strain - induced magnetic phase transition from an AFM insulator to a half metallic ferromagnetic (HM – FM) state is available by the tetragonal distortion due to the insulator – half metallic transition. The predicted electronic and magnetic properties of strain - induced $RbMnF_3$ show the HM – FM nature, making strain – induced $RbMnF_3$ suitable for spintronic application.

PACS numbers: 71.15.Mb, 75.30.Et, 75.50.Ee

I. INTRODUCTION

Although the most common perovskite compounds contain oxygen, there are few perovskite compounds that form without oxygen. The perovskite oxide (e.g., $BiFeO_3$, $BaTiO_3$, $SiTiO_3$ etc) are known to undergo ferro – or antiferro - electric phase transitions, which are accompanied by distortion of the lattice to a lower crystallographic symmetry [1]. Many of the alkali transition metal fluorides (e.g., $KMnF_3$, $RbFeF_3$, $KCoF_3$ etc) undergo similar phase transitions, which are apparently not associated with ferroelectric ordering [2–4]. After the discovery of antiferromagnetism for rubidium trifluoromangate ($RbMnF_3$) [5], the elastic and magnetoelastic properties, nuclear acoustic resonance, magnetostriction and magnetocrystalline anisotropy (MCA) of single crystal AFM $RbMnF_3$ have experimentally investigated [6–10], and the magnetostriction and magnetoelastic couplings were measured at the 4.2 K in the magnetic fields up to 137 kOe [9]. The theoretical and experimental investigations of Mn K – edge for $RbMnF_3$ have shown the behaviors of 3d – 4p intra – atomic interaction in the conduction bands by resonant X – ray magnetic scattering (RXMS) [11, 12].

In order to deeply understand the behavior of fluoroperovskite, the spintronic character and specially the magnetic properties of the $RbMnF_3$ compounds were studied by the first – principles calculations [13]. The AFM materials have been considering renewed attention due to the emerging materials of AFM spintronics [14–20]. Commonly employed to pin the magnetization of an adjacent FM layer in spin valve devices through

*Electronic address: tsogbadrakh@num.edu.mn

the interfacial exchange bias [21–23], among other developments AFM materials have been recently been shown to be efficient spin current detectors by meaning of the spin Hall effect [24, 25]. Three AFM materials that attracted considerable attention in the past are the following fluoride insulators: FeF_2, MnF_2 and $RbMnF_3$. These compounds show simple three dimensional AFM ordering with two sublattices at the temperatures below the Neel temperature of 78, 67 and 83 K respectively [26]. Therefore, these insulators are not directly used to the AFM spintronics due to the low Neel temperatures, and are shown to be the paramagnetic (PM) phase at the room temperature.

The magnetic interactions of FeF_2, MnF_2 and $RbMnF_3$ insulators are dominated by nearest neighbor exchange having effective exchange fields on the same order of magnitude 540, 515 and 830 kOe respectively [26]. However, their magnetic anisotropy fields are different by several orders of magnitude. In FeF_2 compound, the ground state configuration of its magnetic Fe^{2+} ions creates the $^5D_4$ term, which has a finite orbital angular momentum and consequently a large effective anisotropy field of 190 kOe, arising from the spin – orbit coupling of single ion [27, 28]. But in MnF_2 and $RbMnF_3$ compounds, the ground state configuration of their magnetic Mn^{2+} ions creates the $^6S_{5/2}$ term with no single ion angular momentum, so that their crystalline anisotropy is small. In MnF_2, the tetragonal arrangement of the magnetic ions results in a sizable anisotropy of 10 kOe due to the dipolar interaction [29, 30]. However, $RbMnF_3$ has a cubic perovskite structure with no measurable distortion, so that dipolar anisotropy vanishes. As this result, cubic perovskite $RbMnF_3$ has the very small magnetic anisotropy of 4.5 Oe [5]. Recently Lopez Ortiz was shown to occur the AFM – spin flop (SF) and SF – FM transitions due to the very small magnetic anisotropy, and obtained the critical magnetic field and SF temperature for the transition from the AFM phase to the SF phase [10].

In this study, we consider to occur the insulator – half metallic transition of strain – induced perovskite $RbMnF_3$ driving by tetragonal distortion by the first - principles calculations within the framework of spin polarized density functional theory (DFT). Our results have shown the influence of tetragonal distortion to the magnetic property of strain – induced perovskite $RbMnF_3$.

II. COMPUTATIONAL METHOD

The $RbMnF_3$ usually crystallizes in the cubic perovskite structure with the space group of Pm – 3m (# 221). The unit cell of $RbMnF_3$ has the 5 atoms and the atomic positions in $RbMnF_3$ are sited as follows: Rb atom at the (0, 0, 0), Mn atom at the (1/2, 1/2, 1/2), and F atoms at the (0, 1/2, 1/2), (1/2, 0, 1/2), (1/2, 1/2, 0). In order to create the AFM state, we used the (1 x 1 x 2) supercell in all the calculations.

Our calculations are based on the pseudopotential projector augmented wave (PAW) and plane wave (PW) self – consistent field methods using the generalized gradient approximation (GGA) by Perdew, Burke and Ernzerhof (PBE) [31] within the framework of DFT [32, 33], as implemented in the QUANTUM ESPRESSO 6.3 package [34, 35]. The interactions between the ions and valence electrons are expressed as the non relativistic ultrasoft [36] and PAW [37] pseudopotentials taken from the Pslibrary 1.0.0 utility generated by A. Dal Corso [38, 39]. The following electronic states are treated as valence states: Rb($4s^2$, $4p^6$, $5s^1$), Mn($3s^2$, $3p^6$, $3d^5$, $4s^2$) and F($2s^2$, $2p^5$). The wave functions are expressed as plane waves up to a kinetic energy cutoff of 40 Ry and the kinetic energy cutoff for charge density and potential is chosen by 320 Ry.

Three - dimensional Fast Fourier Transform (FFT) meshes for charge density, SCF potential and wavefunction FFT and smooth part of charge density are chosen to be (60 x 60 x 120) grids. There might be need to use finer k – points meshes for a better evaluation of on - site occupations due the strong correlated system. The summation of charge densities is carried out using the special k – points restricted by the (10 x 10 x 5) grids of Monkhorst – Pack scheme due to the computer power ability [40]. The linear tetrahedral method is used when the electronic densities of state (DOS) are evaluated [41]. To obtain optimized atomic structures, ionic positions and lattice parameters are fully relaxed until the residual forces are less than 0.05 eV/$\AA$ for each atom. The occupation numbers of electrons are expressed Gaussian distribution function with an electronic temperature of kT = 0.02 Ry. The mixing mode of charge density is chosen to be local density dependent Tomas – Fermi (TF) screening for highly inhomogeneous systems. Its mixing factor for self – consistency is to be 0.2 and the number of iterations used in mixing scheme is 5. The generalized eigenvalue problem is solved by the iterative diagonalization using the conjugate gradient (CG) minimization technique, and the starting wave function is chosen from superposition of atomic orbitals plus a superimposed "randomization" of atomic orbitals in all our calculation [34, 42]. In order to express the strong correlated effect of electrons in the Mn(3d) state, we first checked the U parameter of Hubbard – based Hamiltonian on – site Coulomb interaction from 2 eV to 7 eV, and was chosen to be U = 5 eV the using the simplified rotational – invariant formulation based on the linear – response method [43]. Atomic wavefunctions used for GGA + U projector are not orthogonalized. In order to perform the MCA calculations [44–46], we have done the spin polarized density functional total energy calculations of non collinear magnetism (GGA + SOC) including the spin – orbit coupling, using the fully relativistic ultrasoft and PAW pseudopotentials taken from the Pslibrary 1.0.0 utility.

III. RESULTS AND DISCUSSION

We have first done the full relaxed total energy calculations of nonmagnetic (NM), FM and AFM states using both the PW and PAW methods by GGA and GGA + U approaches. We presented the results of predicted lattice parameters, band gap, magnetic energy gain between the FM and AFM states ($\Delta E = E_{FM} - E_{AFM}$), magnetic moments per atom and total magnetization of magnetic ions of $RbMnF_3$ on Table I.

TABLE I: The predicted lattice parameters, band gap, magnetic energy gain between the FM and AFM states ($\Delta E = E_{FM} - E_{AFM}$), magnetic moments per atom and total magnetization of magnetic ions of $RbMnF_3$ using the PW and PAW methods by the GGA, GGA + U and GGA + SOC (U = 5.0 eV for Mn ion) approaches.

	PW			PAW		
	GGA	GGA + U	GGA + SOC	GGA	GGA + U	GGA + SOC
a($\AA$)	4.16	4.10	4.30	4.16	4.04	4.30
E_g(eV)	1.28	3.00		1.14	2.92	
ΔE(meV/cell)	24.49	6.04	23.17	26.72	11.16	19.05
M(Mn_1)(μ_B/atom)	4,69	4.79	4.21	4.49	4.77	4.20
M(Mn_2)(μ_B/atom)	-4,69	-4.79	-4.21	-4.49	-4.77	-4.20
M_{tot}(μ_B/cell)	0.00	0.00	0.00	0.00	0.00	0.00

Our results are shown that the ground state of cubic perovskite $RbMnF_3$ is antiferromagnetically stable. In the PW and PAW methods, the AFM state is found to be energetically more stable by 24.49 and 26.72 meV/cell, respectively, than the FM one due to the super - exchange mechanism through Mn – F – Mn bonding by the GGA approach. In these cases, the lattice parameter is predicted to be 4.16 $\AA$, and these values agree with the experimental values of 4.24 $\AA$ [47]. The magnetic moment of Mn ion is found to be 4.69 μ_B/atom by both the methods. But the band gaps are found to be 1.28 and 1.14 eV by the PW and PAW methods respectively. These values are different from the experimental value of 2.50 eV for cubic perovskite $RbMnF_3$ [12]. Therefore, we considered the strong correlated effect of magnetic Mn ion by the U parameter of Hubbard – based Hamiltonian on – site Coulomb interaction.

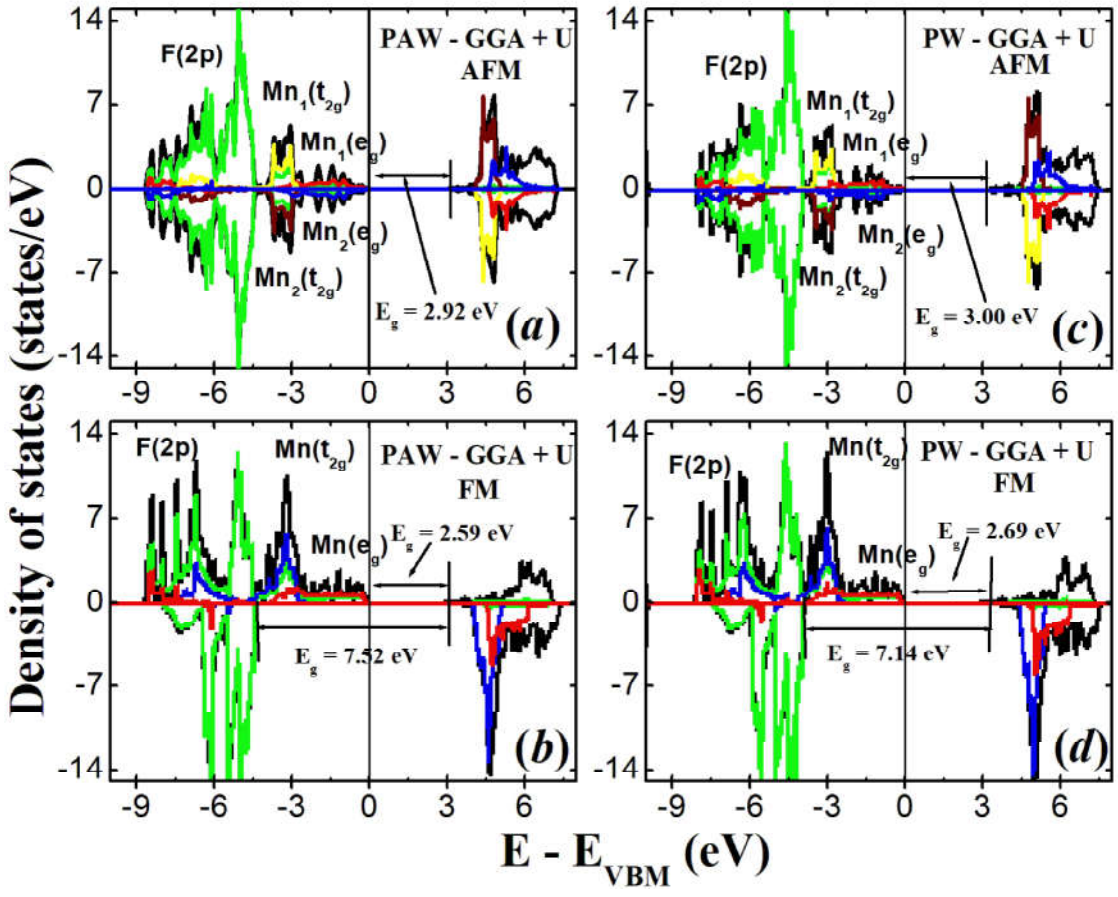

FIG. 1: (Color online) The total and orbital projected electronic densities of states (TDOS and PDOS) of $RbMnF_3$ using the PW and PAW methods by the GGA + U approach. The valence band maximum (VBM) corresponds to the zero.

For the GGA + U approach, the band gaps are found to be 3.00 and 2.92 eV by the PW and PAW methods respectively. It is shown an insulating behavior for both the majority and minority channels. We have shown the electronic total and orbital projected densities of state (TDOS and PDOS) of AFM and FM states for cubic perovskite $RbMnF_3$ using the PAW and PW methods by the GGA + U approach in the Figures (1a, 1b) and (1c, 1d) respectively. The electronic structure of GGA approach is similar to that of GGA + U approach. These values of band gap of AFM state for cubic perovskite $RbMnF_3$ agree with the

other theoretical value of cubic perovskite $RbMnF_3$ [12]. In this case, we note that the magnetic moments increase up to 4.79 and 4.77 μ_B/atom by the PW and PAW methods respectively. The magnetic energy gains are found to be 6.04 and 11.16 meV/cell by the PW and PAW methods respectively. It is shown that the magnetic energy gain decreases, as included the strong correlated effect of magnetic Mn ion. These results affect to the lattice parameter and predicted lattice parameter decreases up to 4.10 and 4.04 $\mathring{A}$ by the PW and PAW methods respectively.

For the AFM state, the Mn(3d) states are symmetrically and are splitting to the Mn(t_{2g}) and Mn(e_g) states by the octahedral crystal field of F ions. The F(2p) state is spreading from -8.6 eV to -2.4 eV and hybridized with the Mn(t_{2g}) state of Mn ion in both the PW and PAW methods. The main peaks of F(2p) states are sited at the positions of -4.6 eV and -5.0 eV by the PW and PAW methods respectively. The Mn(e_g) state is located above the Mn(t_{2g}) state of Mn ion. For the unoccupied states, the separation of unoccupied Mn(t_{2g}) and Mn(e_g) states is to be smaller than that of occupied states. The intra - atomic exchange splitting (Hund's coupling) is larger than the band gap of cubic perovskite $RbMnF_3$. For the FM state the majority and minority states are unbalancing and the band gap of minority state is increasing up to 7.14 and 7.52 eV by the PW and PAW methods respectively. These values are shown to be an insulating behavior for the minority channel. But the band gap of majority state is decreasing up to 2.69 and 2.59 eV by the PW and PAW methods respectively. It is shown a semiconducting behavior for the majority channel. These results agree with the theoretically results by Hashmi [13].

For the PW and PAW methods by the GGA + SOC approach, the lattice parameter is increasing up to 4.30 $\mathring{A}$. The magnetic energy gains between the FM and AFM states are found to be 23.17 and 19.05 meV/cell, and the AFM state is favored to be the ground state of cubic perovskite $RbMnF_3$. The magnetic moments of magnetic ions is found to be 4.21 and 4.20 μ_B/atom in the GGA + SOC approach by the PW and PAW methods respectively. These results are similar to the above results. While the GGA + SOC approach shows that the SOC is not small and it is affected to the lattice parameter of cubic perovskite $RbMnF_3$.

The theoretical work is shown that the bulk modulus of cubic perovskite $RbMnF_3$ is smaller than that of other cubic perovskites $RbXF_3$ (X = V, Co and Fe) [13]. Therefore we created the tetragonal distortion along the c – axis to the cubic perovskite $RbMnF_3$ and the total energy calculations of NM, FM and AFM states have performed at the predicted volume. The magnetic energy gain and magnetic moments of Mn ion are shown in Figures (2a) and (2b) by the GGA and GGA + U approaches respectively. For the tetragonal distortion, when the ratio of c and a parameters becomes greater than 1.2 and 1.3 by the PW and PAW methods respectively, the FM state is favored due to the insulator – half metal transition. We have shown the PDOS of Mn(3d) state in Figures (2c) and (2d) using the PAW and PW methods by the GGA + U approach respectively. The broadening of majority Mn(e_g) state for Mn ion is filling the majority band gap and crossing the Fermi level. The band gap of minority state is reduced up to 5.03 and 5.08 eV by the PAW and PW methods by the GGA + U approach respectively. This strain – induced $RnMnF_3$ is shown a half metal behavior by tetragonal distortion. The magnetic moment of Mn ion is decreasing up to 3.79 and 3.71 μ_B/atom by the PW and PAW methods by the GGA + U approach respectively. We have shown the TDOS of NM state for strained induced $RbMnF_3$ by the PAW and PW methods into the insets of Figures (2c) and (2d) respectively. From our MCA calculations, the magnetocrystalline energy (MCE) defined as

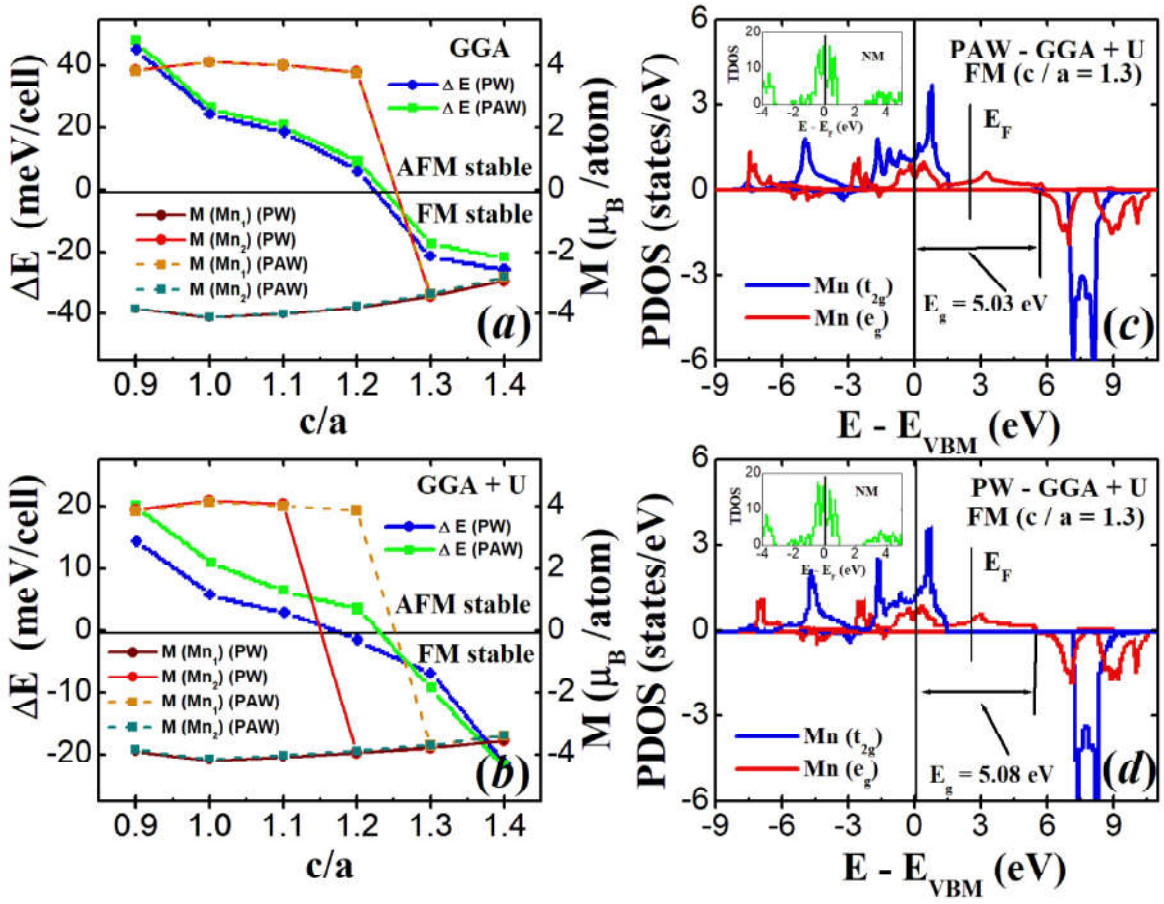

FIG. 2: (Color online) The magnetic energy gains between the FM and AFM states ($\Delta E = E_{FM} - E_{AFM}$) and magnetic moments of $RbMnF_3$ using the PW and PAW methods by the (a) GGA and (b) GGA + U approaches respectively. The orbital projected electronic densities of states (PDOS) of Mn (3d) state for strain – induced perovskite $RbMnF_3$ (by the tetragonal distortion of c / a = 1.3) using the (c) PAW and (d) PW methods by the GGA + U approach respectively. The VBM of minority state corresponds to the zero. For the inserted figures, the total density of state (TDOS) of NM states for strain induced $RbMnF_3$ using the (c) PAW and (d) PW methods by the GGA + U approach respectively. The Fermi energy corresponds to the zero.

($E_{[100]/[010]/[110]} - E_{[111]}$) is found to be 90 meV/cell and the ground state energy of magnetic orientation along the [111] direction is lower than that of other magnetic orientations along the [100], [010] and [110] directions. Therefore, we predicted the easy axis to be along the [111] direction in the strain – induced perovskite $RbMnF_3$ created by the tetragonal distortion with the c/a of 1.3, and it agrees with the easy axis of cubic perovskite $RbMnF_3$ [9]. In finally, we should note that the all results of the PAW methods by GGA, GGA + U and GGA + SOC approach are indicated to occur the insulator – half metal transition by the tetragonal distortion. It is shown that the HM – FM state is favored by the Stoner mechanism of itinerant electrons. This behavior of strain – induced $RbMnF_3$ show the HM – FM nature, making strain – induced $RbMnF_3$ suitable for spintronic application.

IV. CONCLUSION

In conclusion, we have predicted that the ground state of cubic perovksite $RbMnF_3$ is an AFM insulator due to the super – exchange mechanism. After tetragonal distortion along the c – axis, keeping the predicted volume, our results indicated that the strain – induced magnetic phase transition from a AFM insulator to a HM – FM state occurs by the insulator - half metallic transition. We predicted the easy axis to be along the [111] direction in the strain – induced perovskite $RbMnF_3$, and it agrees with the easy axis of cubic perovskite $RbMnF_3$. The predicted electronic and magnetic properties of strain - induced $RbMnF_3$ show the HM – FM nature, making strain – induced $RbMnF_3$ suitable for spintronic application.

Acknowledgments

This work has supported by the research project of the Asia Research Center (Korean Foundation for Advanced Studies), the National University of Mongolia (code P2017-1303 and P2017-2407) and Fundamental research project SSA_014/2016 funded by the Mongolian Foundation for Science and Technology. We thanks for performing the calculations on the server computers at the School of Applied Science and Engineering and Nuclear Physics Research Center in the National University of Mongolia.

[1] F. P. Jona and G. Shirane, Ferroelectric Crystals, Pergamon Press, New York, Chap. V (1962).

[2] O. Beckman and K. Knox, Phys. Rev. **121**, 376 (1961).

[3] L. R. Testardi, H. J. Levinstein and H. J. Gugenheim, Phys. Rev. Lett. **19**, 503 (1967),

[4] J. D. Axe and G. D. Pettit, Phys. Rev. **157**, 435 (1967).

[5] D. T. Teaney, M. J. Freiser and R. W. H. Stevenson, Phys. Rev. Lett. **9**, 212 (1962).

[6] R. L. Melcher and D. I. Bolef, Phys. Rev. **178**, 178 (1969).

[7] R. L. Melcher and D. I. Bolef, Phys. Rev. **186**, 491 (1969).

[8] R. L. Melcher and D. I. Bolef, Phys. Rev. **184**, 556 (1969).

[9] Y. Shapira and N. F. Oliveira Jr, Phys. Rev. B **18**, 1425 (1978).

[10] J. C. Lopez Ortiz, G. A. Fonseca Guerra, F. L. A. Machado and S. M. Rezende, Phys. Rev. B **90**, 054402 (2014).

[11] A. Stunault, F. de Bergevin, D. Wermeille, C. Vettier, Th. Bruckel, N. Bernhoeft, G. J. McIntyre and J. Y. Henry, Phys. Rev. B **60**, 10170 (1999).

[12] M. Taguchi and M. Altarelli, J. Electron Spectroscopy and Related Phenomena **136**, 205 (2004).

[13] M. R. Hashmi, M. Zafar, M. Shakil, A. Sattar, S. Ahmed and S. A. Ahmad, Chin. Phys. B **25**, 117401 (2016).

[14] A. S. Nunez, R. A. Duine, P. Haney and A. H. MacDonald, Phys. Rev. B **73**, 214426 (2006).

[15] A. B. Shick, S. Khmelevskyi, O. N. Miryasov, J. Wunderlich and T. Jungwirth, Phys. Rev. B **81**, 212409 (2010).

[16] A. H. MacDonald and M. Tsoi, Philos. Trans. R. Soc,, A **369**, 3098 (2011).

[17] V. M. T. S. Barthem, C. V. Colin, H. Mayaffre, M. -H. Julien and D. Givord, Nat. Commun. **4**, 2892 (2013).

[18] P. Merodio, A. Ghost, C. Lemonias, E. Gautier, U. Ebels, M. Chshiev, H. Bea, V. Balz and W. E. Bailey Appl. Phys. Lett. **104**, 032406 (2014).

[19] C. Hahn, G. de Loubens, V. V. Naletov, J. B. Youssef, O. Klein and M. Viret, arXiv: 1310.6000 (2013).

[20] E. V. Gomonnay and V. M. Loktev, Low Temp. Phys. **40**, 17 (2014).

[21] S. S. P. Parkin **et. al.**, J. Appl. Phys. **85**, 5828 (1999).

[22] J. Nogues and I. K. Schuller, J. Magn. Magn. Mater. **192**, 203 (1999).

[23] J. R. Fermin, M. A. Lucena, A. Azevedo, F. M. de Aguiar and S. M. Rezende, J. Appl. Phys. **87**, 6421 (2000).

[24] H. Chen, Q. Niu and A. H. MacDonald, Phys. Rev. Lett. **112**, 017205 (2014).

[25] J. B. S. Mendes, R. O. Cunha, O. Alves Santos, P. R. T. Ribeiro, F. L. A. Machado, R. L. Rodrigues – Suarez, A. Azevedo and S. M. Rezende, Phys. Rev. B **89**, 140406(R) (2014).

[26] L. J. de Jongh and A. R. Miedema, Adv. Phys. **50**, 947 (2001).

[27] R. C. Ohlmann and M. Tinkham, Phys. Rev. **123**, 425 (1961).

[28] M. T. Hutchings, B. D. Rainford and H. J. Guggenheim, J. Phys. C **3**, 307 (1970).

[29] F. Keffer, Phys. Rev. **87**, 608 (1952).

[30] J. Barak, V. Jaccarino and S. M. Rezende, J. Magn. Magn. Mater. **9**, 323 (1978).

[31] J. P. Perdew, K. Burke and M. Ernzerhof, Phys. Rev. Lett. **77**, 3865 (1996).

[32] P. Hohenberg and W. Kohn, Phys. Rev. **136**, B864 (1964).

[33] W. Kohn and L. J. Sham, Phys. Rev. **140**, A1133 (1965).

[34] P. Gianmozzi, S. Baroni, N. Bonini, M. Calandra, R. Car, C. Cavazaaoni, D. Ceresoli, G. L. Chiarotti, M. Cococcioni, I.Dabo, A. D. Corso, S. de Gironcoli, S. Fabris, G. Fratesi, R. Gebauer, U. Gerstmann, C. Gougoussis, A. Kokalj, M. Lazzeri, L. Martin-Samos, N. Marzari, F. Mauri, R. Mazzarello, S. Paolini, A. Pasquarello, L. Paulatto, C. Sbraccia, S. Scandolo, G. Sclauzero, A. P. Seitsonen, A. Smogunov, P. Umari and R. M. Wentzcovich, J. Phys.: Condens. Matter **21**, 395502 (2009).

[35] P. Giannozzi, O. Andreussi, T. Brumme, O. Bunau, M. Buongiorno Nardelli, M. Calandra, R. Car, C. Cavazzoni, D. Ceresoli, M. Cococcioni, N. Colonna, I. Carnimeo, A. Dal Corso, S. de Gironcoli, P. Delugas, R. A. DiStasio Jr, A. Ferretti, A. Floris, G. Fratesi, G. Fugallo, R. Gebauer, U. Gerstmann, F. Giustino, T. Gorni, J Jia, M. Kawamura, H.-Y. Ko, A. Kokalj, E. Kucukbenli, M .Lazzeri, M. Marsili, N. Marzari, F. Mauri, N. L. Nguyen, H.-V. Nguyen, A. Otero – de-la – Roza, L. Paulatto, S. Ponce, D. Rocca, R. Sabatini, B. Santra, M. Schlipf, A. P. Seitsonen, A. Smogunov, I. Timrov, T. Thonhauser, P. Umari, N. Vast, X. Wu, S. Baroni, J.Phys.: Condens. Matter **29**, 465901 (2017).

[36] D. Vanderbilt, Phys. Rev. B **41**, R7892 (1990).

[37] P. Blochl, Phys. Rev. B **50**, 17953 (1994).

[38] Andrea Dal Corso, Computational Materials Science **95**, 337 (2014).

[39] E. Kucukbenli, M. Monni, B. I. Adetunji, X. Ge, G. A. Adebayo, N. Marzari, S. de Gironcoli, and A. Dal Corso, arXiv:1404.3015v1 (2014).

[40] H. J. Monkhorst and J. D. Pack, Phys. Rev. B **13**, 5188 (1976).

[41] P. E. Blochl, O. Jepsen and O. K. Andersen, Phys. Rev. B **49**, 16223 (1994).

[42] M. C. Payne, M. P. Teter, D. C. Allan, T. A. Arias and J. D. Joannopoulos, Rev. Mod. Phys. **64**, 1045 (1992).

[43] M. Cococcioni and S. de Gironcoli, Phys. Rev. B **71**, 035105 (2005).

[44] G. Autes, C. Barreteau, D. Spanjaard and M. Desjonqueres, J. Phys.: Condens. Matter **18**, 6785 (2006).

[45] D. Li, A. Smogunov, C. Barreteau, F. Ducastelle, and D. Spanjaard, Phys. Rev. B **88**, 214413 (2013).

[46] X. B. Liu, Z. Altounian and D. H. Ryan, J. Alloys and Compounds **688**, 188 (2016).

[47] R. L. Moreira and A. Dias, J. Phys. Chem. Solids **68**, 1617 (2007).

Characterization study of coal spontaneous combustion by EPR spectroscopy

Munkhtsetseg Sambuu,* Galbadrakh Ragchaa, Enkhtur Lkhamsuren, and Erdene-Ochir Ganbold
Department of Physics, School of Sciences and Arts,
The National University of Mongolia, University Street-1, 14201 Ulaanbaatar, Mongolia

In the present paper the low temperature (up to 200^0C) treatment to the coal was examined by the EPR spectroscopy. Among the studied coals KhT and Kho coals were more temperature reactive showing greater concentration and broader EPR spectra from environmentally persistent free radicals (EPFRs).

PACS numbers: 89.30.ag, 76.30.-v, 07.57.Pt

I. INTRODUCTION

The existence of coal free radicals was recognized first in 1950s by Ingram et al., [1] by using Electron Spin Resonance (ESR) or Electron Paramagnetic Resonance (EPR) spectroscopy, since the method was found its opportunity in the study of coal characterization with broad spectra.

Coals are actively interacted with oxygen and halogens. The reaction of coal with atmospheric oxygen or pyrite, or an adsorption of water molecules on its surface may appear at an ambient temperature that causes self-oxidation as described a spontaneous combustion of coal.

The coal that is treated by the heat goes through a decomposition of the organic substances is as defined pyrolysis whose mechanism is literally assumed the existence of temporary fragments of molecules or free radicals [2]. The formation of free radicals during heating of coal is approved quite early and discussed by many authors [2–10]. Free radicals that formed by bond cleavage are the main intermediates during coal pyrolysis. Thus the determination of characteristics of these radicals then becomes as highly important as the reaction itself in the thermal decomposition or the study of mechanism of compound evolution. The concentration of free radicals of coal declined to the spontaneous combustion is notably changes in the oxidation which refers the main role of radicals in the process.

Free radicals can be detected using the EPR method if they are maintained at steady-state. The method advantages are included high sensitivity, non-destructive way of study, minor dosage and broad detection in the study of free radicals in coals.

During oxidation it is both absorption of oxygen and yield of oxidation productions like H_2O, CO_2 and CO, so there are two types of radicals, carbon or oxygen centered, draw the EPR spectra. These spectra of the free radicals subsequently differ from their EPR parameters like g-value, linewidth, and intensity. Moreover, due to the substantial heterogeneity of coal structure, electron spin magnetic moments are affected by the microwave power in some level. Another factors that can be regarded influenced by free radicals are coal

*Electronic address: munkhtsetseg_s@num.edu.mn

chemical constitution and coal coalification degree.

In the present paper the low temperature (up to 200^0C) treatment to the coal was examined by the EPR spectroscopy.

II. EXPERIMENTAL

Sample preparation. Coal sample description, preparation and its elemental analysis results are taken from [11]. Consequently, coal samples from Baganuur (abbreviated as Ba), Nalaikh (as Na), Sharyn-Gol (as ShG), Khotgor (as Kho), Khartarvagatai (as KhT) and Tavantolgoi (as TT) were chosen in the current work. Sample mass is measured on the Ohaus explorer E10640 micro balance and sample size on Konus # 5420 Diamond Stereomicroscope with $20x - 40x$ magnification.

Heat treatment to coal and EPR measurement. In the first experiment the heat treatment up to 200^0C was done directly on the EPR spectrometer resonator. EPR measurement was performed at about 9.4 GHz with a Bruker spectrometer equipped with continuous nitrogen flow cryostat to study temperature dependence from room temperature (20^0C) up to 200^0C. Solid samples were sealed directly into glass tubes (with mass of approximately 10-30 mg) and measured firstly in wide range of sweep field ($\approx$ 5000 Gs) and then central resonance field repeatedly. A time of keeping each coal samples in that exact temperature is taken 20 mins. EPR spectra were then registered at every 50^0C. For every coal sample it is also registered a signal at room temperature when cooled from 200^0C which was approximately after 30 mins.

To the estimated value of the radical concentration of the coals at different temperature the correction was made by using the concentration of a reference sample (pitch, g = 2.0028 and $N_{ref} = 6.06 \times 10^{15}$ spin) measured at room temperature by applying the Boltzmann distribution of radicals between ground and excited states that varies with temperature:

$$I_{abs} = \frac{N_{abs}}{m_{sample}} = \frac{N_{ref}}{m_{sample}} \cdot \frac{(T_{sample} - \theta_{sample})I_{sample}}{(T_{ref} - \theta_{ref})I_{ref}} \tag{1}$$

where I_{sample} and I_{ref} are the sample and reference-signal intensity, respectively, T is the temperature under which the experiment was conducted, N is the number of radicals, and m_{sample} is the sample mass. The Weiss temperature θ was neglected due to the $T \gg \theta$ for these coal type of radicals.

III. RESULT AND DISCUSSION

It has been established that coal contains oxygenated complexes even in as received form. During the thermal treatment (low temperature) the released carbon oxide can be detected by spectroscopically.

EPR is sufficient sensitive to very small variation in the electronic structure therefore, EPR signals from similar characteristics coals like Ba, Na and ShG that are located in nearby location can be distinguished by linewidth, lineshape and related dependencies on the given temperatures.

All samples were yielded X-band EPR spectra containing one single broad signal at room temperature, however a line shape of the spectra then been changed under using temperature in the range of $50 - 200^0C$.

g-factor, linewidth as means a peak-to-peak distance of the first derivative spectrum or half height width of the absorbance spectrum and radical concentration of the powder coal samples were then determined from the measurement. Asymmetric spectrum was given from Kho coal at all used temperatures. The EPR parameters of Kho coal was determined in [11] at room temperature. After temperature treatment up to 200^0C, each coal sample was cooled directly in the resonator and measured the EPR spectrum at room temperature afterwards. A significant difference in EPR parameters was notified on the spectra of TT and KhT coals.

The most coals (TT, KhT, Kho and Ba) show Curie type temperature dependency of the signal intensity, so that paramagnetic centers were localized caused by breaking bonds like $C-O$, $C-H$ and $C-C$ (fig 1). This increase of the intensity was demonstrative for KhT coal. For ShG and Na coals the signal intensity was weakly depended on the used low temperatures.

As to the elemental analysis result TT coal is only one high rank (or bituminous) with high carbon content coal and the rest are opposite, low carbon content (or brown). It was noticed that KhT coal behaves like TT coal. Its radical concentration was increased significantly than TT from $100-200^0C$ temperature range. For both coals a rapid increase (by an order more) that starts from 100^0C is literally related to the quite stable free radicals and their intrinsic reactivity of chars or stable free radicals complex interplay as a support of broken bond forming free radicals, not depending on the rank of coals. In the result the central part of the signal was narrowing and being sharp intense edged and tails of the signal being gradually dropped in such way that the signal consists a broad line in the tail and a narrow line in the center. The linewidth of the narrow line reaches 0.1 mT from 0.33 mT (KhT) and from 4.4 mT (TT). Kho coal shows similar character a bit later temperature at 150^0C, however this coal's specific radicals were kept during the used temperature. A radical concentration is without hopping but small linear increase for Ba coal. The most unstability of unpaired electrons are in ShG and Na coals. From the hopping values of their radical concentration one could conclude their radicals may undergo coupling reactions before volatile being condensed.

With the current used low temperature range in the direction of increasing g-factor values of the exact coal vary inconsiderably, but it should be noted here a tendency to decrease of g-factor at higher temperature. Because of the inhomogeneity of coal itself it is estimated an error on the g-factor value that of approximately 2×10^{-4}.

g-factor is evaluated as higher value when more unpaired electrons are located in the heteroatoms like O, S and N in coals. g-factor of brown type coals (Na and Ba) are 2.0045 and 2.0042 at room temperature and has no significant change with slightly decreasing down to 2.0042 and 2.0041 during the used temperature range. ShG has the most higher value of g-factor at room temperature among studied coals, though it has dropped abruptly due to the first temperature used, then kept almost constantly.

g-factor values of KhT and Kho coals are lower (2.0038 and 2.0037) and slightly decrease (up to 2.0033 and 2.0034) with the temperature.

An increase of g-factor was detected only on TT coal (from 2.0034 at room temperature to 2.0036 at 150^0C). This increased shift of g-factor can be attributed to the conversion of the material itself. As the result its linewidth also decreases with the temperature.

According to the plot (fig 2) mean value of g-factor of every studied coal relates to that of exact small interval

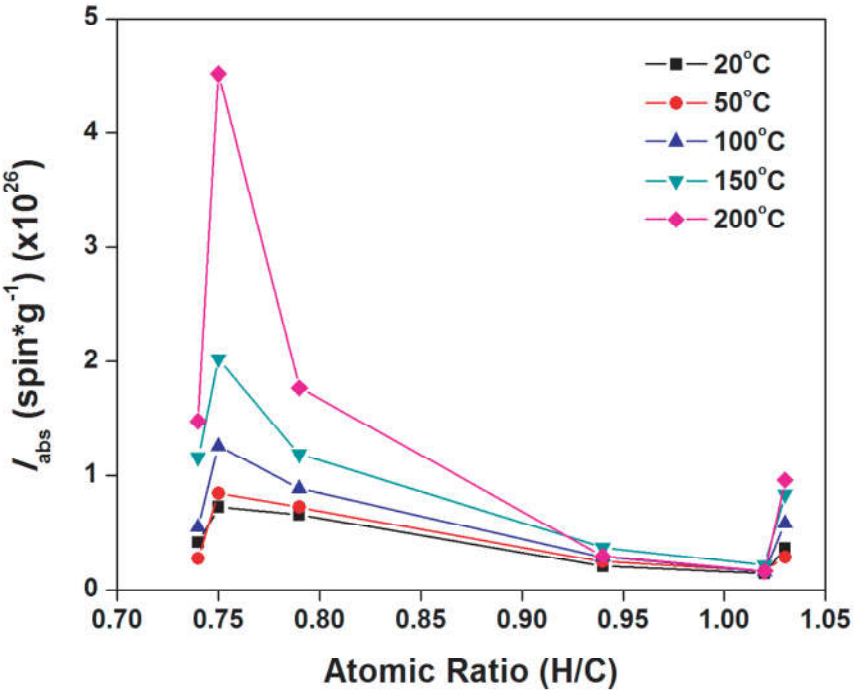

FIG. 1: Effect of used low temperature range on the radical concentration determined as formula (1) and atomic ratio H/C for the studied coals.

of the radical concentration. Therefore, the lowest radical concentration detected but the highest g-factor owned coal is Na and then it goes like ShG, Ba and TT. Kho and KhT coals are showed a smooth decrease in the dependence between g-factor and the temperature or the radical concentration and the temperature. g-factor value shift to lower value then might indicate a formation of redox-active transition metal oxide nanoparticles such as copper and iron oxides, subscribed as environmentally persistent free radicals (EPFRs), that was mentioned in the works of Dellinger et al., [12, 13] on the coal surface due to temperature. These combustion-generated particles are actively participated in the formation of organic precursors.

Linewidth of the EPR spectra of the studied coals that refers an interaction of radical and its environment was a bit above and below 0.7 mT for brown coals like Ba (0.59 mT), Na (0.76 mT), ShG (0.75 mT). Narrower lines are TT and Kho (0.44 mT) and KhT (0.33 mT). The temperature influences to the linewidth of TT, KhT and Kho coals becoming more narrower but less and almost not changing for Na and ShG. The linewidth of Ba coals slightly increases with a rise of the temperature. A slow increase of Ba coal linewidth is a point-to-point related to the radical concentration curve, thereof an interaction of the electrons is strengthened by a formation of radicals caused by the temperature. A similar conclusion also can be made for ShG and Na coals dependence curves. For TT, KhT and Kho coals a continuous decrease of the linewidth is connected to their chemical structural changes due to the used temperature. Particularly, an appearance of a narrow line in the center of the spectrum for coals was considered as changes in the composition of the coals that called by oxygen and coal interaction, consequently, the narrow line is from fusinite part and the broad line from

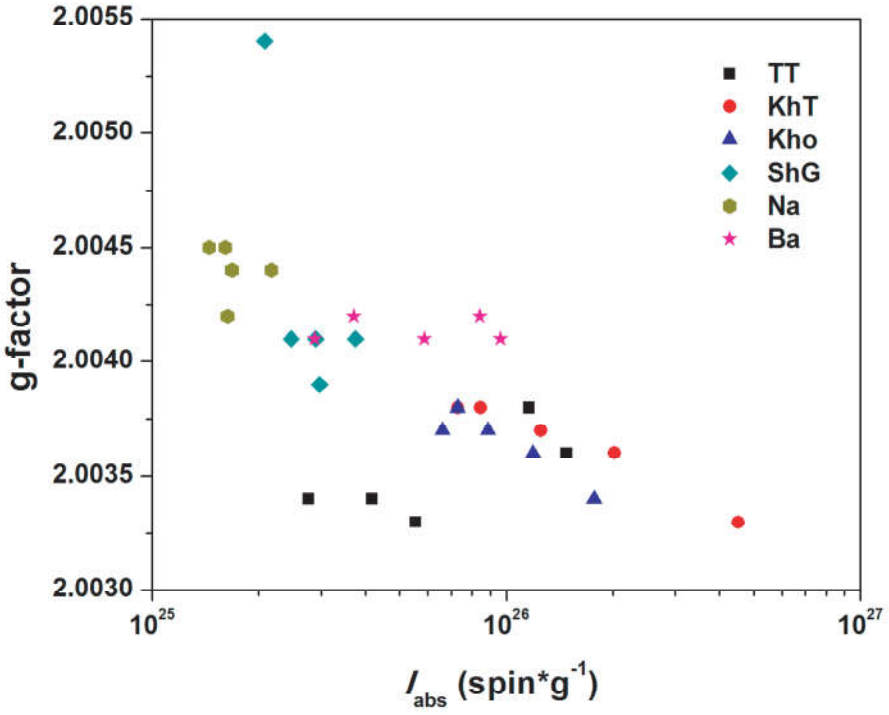

FIG. 2: Plot of the g-factor vs used temperatures for the studied coals.

vitrinite.

Lineshape has been significantly changed depending on the used temperature range for TT and KhT coals. EPR spectrum of KhT at room temperature (symmetric, low intense and with g-factor of 2.0038) has been turned into the asymmetric, intense with g-factor of 2.0033 at 200^0C.

Therefore, information of EPR spectra are confirmed the metal oxides formation and activation on the coal surface during heat treatment. From this point of view, an inversion of EPR spectra can be explained as following: Transition metal oxides perform successfully as semiconductors at room temperature.

KhT coal distinguished by its unique characteristics at low temperature combustion in the first experiment set that behaves like an bituminous coal like TT. Higher carbon concentration coals like bituminous and antracites own specific electric conductivity that depends on the sample size in which result an inversion of the EPR signal by a phase change in ultra high frequency wave magnetic component [14].

IV. CONCLUSION

EPR spectra of coals treated with low temperature were obtained to study the characterization of spontaneous combustion of coal.

During the heat treatment there are formed intermediate radicals whose concentration follows Curie law for TT, KhT, Kho and Ba coals. But Na and ShG coals the radical concentration remained unchanged in the increasing of the temperature.

g-factor tends to decrease for the most coals (KhT, Kho, ShG, Na and Ba) excluding high rank coal of TT. Linewidth of EPR spectra is varied into decreasing direction of value. TT and KhT coals line shape gives significant change due to the temperature.

Acknowledgments

This work was supported by the project #P2016-1216 from the Asian Research Center in Mongolia.

[1] Ingram D.J.E., Tapley J.G., Jackson R., Bond R.L., Murnahgan A.R., Nature (London). 1954, 174, p.797

[2] Walter Fuchs, A. G. Sandhoff. Industrial and engineering chemistry. 1942, 34, p. 567-571.

[3] W. B. Davies, D. J. Brown. Brown Nature. 1967, p. 64-65.

[4] Neavel, R. C. Fuel. 1976, 55, p. 237-242.

[5] L. Petrakis, D. W. Grandy. Nature. 1981, 289, p. 476-477.

[6] Soon Sam Kim, Mark L. Jarand, Kandaswamy Durai-Swamy. Fuel. 1982, 61 (11), p. 1124-1126.

[7] Richard F. Sprecher, Herbert L. Retcofsky. Fuel. 1983, 62(4), p. 473-476.

[8] Timothy G. Fowler, Keith D. Bartle, Rafael Kandiyoti. Fuel. 1987, 66, p. 1407-1412.

[9] J. Kudynska, H. A. Buckmaster. Fuel. 1993, 72(12), p. 1733-1738.

[10] H. Wang, B. Z. Dlugogorski, E. M. Kennedy. Combustion and Flame. 2003, 134, p. 107117

[11] S. Munkhtsetseg, N. M. Lapchuk, N. A. Poklonski, N. I. Gorbachuk, Kh. Tsookhuu, G. Shilagardi, N. Tsogbadrakh, A. N. Oleshkevich. 6^{th} International Conference "Materials and Structures of Modern Electronics" October 8 - 9, 2014, Minsk (Belarus), p. 15-19.

[12] Machael P. Herring, Lawrent Khachatryan, Barry Dellinger. World Acad Sci Eng Technol. 2015, 9(7), p. 804-812.

[13] Barry Dellinger, Slawomir Lomnicki, Lavrent Khachatryan, Zofia Maskos, Randall W. Hall, Julien Adounkpe, Cheri McFerrin, Hieu Truong. Proceedings of the Combustion Institute. 2007, 31(1), p. 521-528.

[14] N. A. Poklonski, S. A. Vyrko, O. P. Poklonskaya, N. M. Lapchuk, S. Munkhtsetseg. Journal of Applied Science. 2013, 80(3), p. 366-371.

Imaginary time density functional calculation of ground states for second – row atoms using CWDVR approach

D. Naranchimeg[1],* L. Khenmedekh[1], G. Munkhsaikhan[1], and N. Tsogbadrakh[2]†

[1] *Department of physics, Mongolian University of Science and Technology, Ulaanbaatar 14191, Mongolia*

[2] *Department of physics, National University of Mongolia, Ulaanbaatar 14201, Mongolia*

We have developed the Coulomb wave function discrete variable representation (CWDVR) method to solve the imaginary time dependent Kohn – Sham equation on the many – electronic second row atoms. The imaginary time dependent Kohn – Sham equation is numerically solved using the CWDVR method. We have presented that the results of calculation for second row Li, Be, B, C, N, O and F atoms are in good agreement with other best available values using the Mathematica 7.0 programm.

PACS numbers: 31.15.p, 31.15.E, 67.90.+z, 71.15.Mb

I. INTRODUCTION

Numerical approach of many – electron systems is extremely difficult computation. Density functional theory (DFT) is a computational quantum mechanical modeling method used to investigate many – electron systems, in particular atoms, molecules, and the condensed phases [1]. It provides a powerful alternative technique to ab – *initio* wave function approach, since the electron density $\rho(\vec{r})$ possesses only three spatial dimensions no matter how large the system is. The DFT proves accurate and computationally much less expensive than usual ab – *initio* wave function methods, such as a Hartree Fock method. However, the exchange – correlation energy functional, which is a functional of the total electron density is not known exactly, and thus approximate exchange – correlation energy functional must be used. The DFT based upon the Hohenberg – Kohn (HK) energy functional [2] focuses on the solution of exchange – correlation energy and it had been used in many calculations of ground state properties an atomic system. The Kohn – Sham equation is shown to be solved by the Coulomb wave function discrete variable representation method. Since the CWDVR method is able to treat the Coulomb singularity naturally, it is suitable for atomic systems [3]. In our previous article, we calculated the ground state properties for noble gas atoms, such as He, Ne and Ar atoms using the Coulomb wave function discrete variable representation (CWDVR) method [4].

In this paper, we present the solution of the Kohn-Sham equation on the ground state problem for the many – electronic second row – atoms by the CWDVR method. This paper consists of methodology and results by the CWDVR method. We show that ground state energy values calculated by the present method are in good agreement with other precise theoretical calculations.

---

*Electronic address: Naranchimeg@must.edu.mn

†Electronic address: Tsogbadrakh@num.edu.mn

II. CWDVR METHOD

The DVR method has its origin in the transformation method devised by Harris et al [5], where it was further developed by Dickinson and Certain [6]. Light et al. [7] first explicitly used the DVR method as a basis representation for quantum problems, where after different types of DVR methods have found wide applications in different fields of physical and chemical problems [8]. The DVR method gives an idea, associated basis functions are localized about discrete values of the coordinate under consideration. The DVR simplifies the evaluation of Hamiltonian matrix elements. The matrix elements of kinetic energy can also be calculated very simply and analytically in most cases [9]. In this section, we first give a brief introduction to the DVR constructed from orthogonal polynomials and Coulomb wave functions, which will be used to solve the Kohn – Sham equation for many – electron atomic systems.

The DVR approach basis functions can be constructed from any complete set of orthogonal polynomials, defined in the domain with the corresponding weight function [9]. It is known that a Gaussian quadrature can also be constructed using nonclassical polynomials. The DVR derived from the Legendre polynomials has been shown by Machtoub and Zhang [10] to provide very precise results for the metastable states of the exotic helium atom.

An appropriate quadrature rule for the Coulomb wave function was given by Dunseath et al [11] with explicit expressions for the weights. The time dependent single particle Kohn – Sham equation has the form

$$i\frac{\partial\psi_j(\vec{r},t)}{\partial t} = (\widehat{H}_0 + \upsilon_{eff})\psi_j(\vec{r},t), j = \overline{1,N} \tag{1}$$

Here, $\psi(\vec{r},t)$ the single particle Kohn – Sham orbit of N electron atom, $\widehat{H}_0$ – atomic Hamiltonian, υ_{eff} is the time dependent effective potential, and charge density depends on the coordinates and time and is given by

$$\rho(\vec{r},t) = \sum_{j=1}^{N} |\psi_j(\vec{r},t)|^2 \tag{2}$$

However, one can rewrite Eq.(1) in imaginary time τ and substitute $\tau = -it$, t being the real time, to obtain a diffusion – type equations:

$$-\frac{\partial R_j(\vec{r},t)}{\partial t} = (-\frac{1}{2}\nabla^2 + \upsilon_{eff})R_j(\vec{r},t) \tag{3}$$

The Kohn – Sham effective local potential contains both classical and quantum potentials and can be written as:

$$\upsilon_{eff}[\rho;\vec{r},t] = \frac{\delta E_{bb}}{\delta\rho} + \frac{\delta E_{ne}}{\delta\rho} + \frac{\delta E_{xc}}{\delta\rho} + \frac{\delta E_{ext}}{\delta\rho} \tag{4}$$

Here the first term is inter – electronic Coulomb repulsion, the second is the electron – nuclear attraction term, the third is exchange – correlation term, and last term comes from interaction with the external field (in the present case, this interaction is zero). A simple local energy functional form has been applied for the atoms, and the exchange part can be found to be [12],

$$\frac{\delta E_x}{\delta \rho} = \frac{\delta E_x^{LDA}}{\delta \rho} - \beta \left[\frac{\frac{4}{3}\rho^{1/3} + \frac{2}{3}\frac{r^2 \rho}{\alpha_x}}{(1 + \frac{r^2 \rho^{2/3}}{\alpha_x})^2} \right] \tag{5}$$

$$\frac{\delta E_x^{LDA}}{\delta \rho} = -\frac{4}{3} C_x \rho^{1/3} \tag{6}$$

The simple local parameterized Wigner – type correlation energy functional [13] used for ground states:

$$E_c = -\int \frac{\rho}{a + b \cdot \rho^{-1/3}} d\vec{r} \tag{7}$$

$$\frac{\delta E_c}{\delta \rho} = -\frac{a + c \cdot \rho^{-1/3}}{(a + b \cdot \rho^{-1/3})^2} \tag{8}$$

where $a = 9.81$, $b = 21.437$, $c = 28.582667$ are respectively. The solution of Eq.(1) is used split time method, for split time Δt. It can be written

$$R(\vec{r}, t + \Delta t) \cong e^{-\Delta t \hat{H}_0/2} e^{-\hat{V} \Delta t} e^{-\Delta t \hat{H}_0/2} R(\vec{r}, t) \tag{9}$$

One of the main features of the DVR is that a function $R(\vec{r}, t)$ can be approximated by interpolation through the given grid points:

$$R(r) \cong \sum_{j=0}^{N} R(r_j) \cdot g_j(r) \tag{10}$$

Here: $R(r_j)$ is the interpolation function, $g_j(r)$ is the cardinal function.

The Coulomb wave function is defined by radial grid points. Interpolation function is obtained by using the radial function that is derived from the cardinal functions. By noting that $F(r)$ is the Coulomb function, $F'(r)$ is the first derivative from F(r) at the position r_j, ψ_j is found to be $\psi_j = \frac{R(r)}{F'(r)}$. The propagation in the energy space (step first in equation) can now be achieved through

$$e^{-\hat{H}_0\Delta t/2}R(r) = \sum_{j=0}^{N} e^{-\hat{H}_0\Delta t/2}R(r_j)g_j(r) \tag{11}$$

The cardinal functions $g_j(r)$ in (Eq.10) are given by the following expression

$$g_j(r) = \frac{1}{F'(r_j)}\frac{F(r)}{r - r_j} \tag{12}$$

where the points r_j $(j = 1, 2, ..., N)$ are the zeros of the Coulomb wave function $F(r)$ and $F'(r_j)$ stands for its first derivative at r_j and $g_j(r)$ satisfies the cardinality condition

$$g_j(r_i) = \delta_{ji}. \tag{13}$$

Since the Coulomb wave functions was expressed in quadrature rule with expressions for the weight ω_j, then DVR basis function $F_j(r)$ satisfies the eigenvalue for the radial Kohn – Sham type equation:

$$\hat{H}(r)\psi(r) = E\psi(r) \tag{14}$$

and

$$\hat{H}(r) = -\frac{d^2}{2d^2} + V(r). \tag{15}$$

The DVR greatly simplifies the evaluation of Hamiltonian matrix elements. The potential matrix elements involve merely the evaluation of the interaction potential at the DVR grid points, where no integration is needed. The DVR basis function $f_j(r)$ is constructed from the cardinal function $g_j(r)$ as follows

$$f_j(r) = \frac{1}{\sqrt{\omega_j}}g_j(r), \tag{16}$$

here the weight ω_j is given in [11]:

$$\omega_j \approx \frac{\pi}{a_j^2}. \tag{17}$$

$$a_j = F'(r_j). \tag{18}$$

The second derivative of the cardinal function $g_j^{''}(r_j)$ is given by

$$g_j^{''}(r_j) = \delta_{jk}\frac{c_k}{3a_k} - (1-\delta_{jk})\frac{a_k}{a_j}\frac{2}{(r_k - r_j)^2}, \tag{19}$$

where a_k is given by Eq.(18) and c_k. Here kinetic energy matrix elements D_{ij} calculated using:

$$c_k = -a_k(2E + 2Z/r), \tag{20}$$

$$D_{ji} = -\delta_{ij}\frac{c_i}{6a_i} + (1-\delta_{ji})\frac{1}{(r_i - r_j)^2}, \tag{21}$$

In the Eq.(15), to expand $R(r_j)$ in the eigenvectors of the Hamiltonian $\hat{H}_0$, we first solve the eigenvalue problem for $\hat{H}_0$ after discretization of coordinate, the differential equation for this problem can be written as:

$$\sum_{j=1}^{N}\Big[-\frac{1}{2}D_{ji} + V(r_j)\delta_{ji}\Big]\phi_{kj} = \varepsilon_k\phi_{kj} \tag{22}$$

Here D_{ji} denotes the symmetrized second derivative of the cardinal function that is given as,

$$(D_2)_{ji} = \frac{1}{3}(E + \frac{Z}{r}), \qquad j = i \tag{23}$$

$$(D_2)_{ji} = \frac{1}{(r_i - r_j)^2}, \qquad j \neq i. \tag{24}$$

The Eq.(2) is then numerically solved to achieve a self – consistent set of orbitals, using the DVR method. These orbitals are used to construct various Slater determinants arising out of that particular electronic configuration and its energies computed in the usual manner. A key step in the time propagation of Eq.(9) is to construct the evolution operator $e^{-\hat{H}_l^0\Delta t/2} \cong S(l)$ through an accurate and efficient representation of $\hat{H}_l^0$. Here we extend the DVR method to achieve optimal grid discretization and an accurate solution of the eigenvalue problem of $\hat{H}_l^0$.

In the present work, we are particularly interested in the exploration of the improvement of the Kohn – Sham type equation in electron structure calculation. Thus we choose the Slater wave function as our initial state at $t = 0$. Note that, the differential equation for time propagation is normalized at the each time step. Here the 152 grid points are used for the DVR discretization of the radial coordinates and $\Delta t = 0.001au.$, with 500 iteration is used in the time propagation to achieve convergence.

III. CALCULATION AND RESULTS

In this section we present results from nonrelativistic electronic structure calculation of the ground states of Li, Be, B, C, N, O and F atoms. Here, parameters of the Coulomb wave function such as wave number and effective charges are chosen to be $k = \sqrt{2E} = 3$ and $Z1 = 400$. Table I summarizes the main results for mentioned atoms. The first row shows the present results. The results from the Amlan K Roy [14] for energies for the ground states for Li, Be, B, C, N, O and F atoms are shown below the present results. The corresponding HF values from the literature are listed for comparison. For all atoms except F (mismatch 3.1%), we found the present results of the total electronic energies are considerably match the HF values and are significantly better than the results from Amlan K Roy [14].

TABLE I: **Calculated ground – state properties of Li, Be, B, C, N, O and F atoms (by the unit of au.) along with literature data for comparison.**

		Li	Be	B	C	N	O	F
$-E$	Present work	7.3197	14.582	24.779	37.9484	55.625	75.795	102.897
	Roy [13]	7.221	14.22 1	23.964	36.953	53.407	73.451	99.734
	HF [2]	7.4332	14.573	24.529	37.688	54.400	74.809	99.400
$-Z/r$	Present work	17.054	33.447	56.728	88.447	128.915	179.317	240.433
	Roy [13]	17.115	34.072	58.143	88.649	127.326	176.324	-
$-E_x$	Present work	1.752	2.656	3.732	5.0416	6.527	8.223	10.147
	Roy [13]	1.574	2.404	3.478	4.640	5.987	7.490	10.000
	HF [2]	1.781	2.667	3.744	5.045	6.596	8.174	10.020
$-E_c$	Present work	0.0659	0.093	0.1252	0.1637	0.2058	0.2524	0.303
	Roy [13]	0.154	0.322	0.302	0.368	0.434	0.543	-
	HF [2]	0.0435	0.094	0.111	0.1560	0.1890	0.2414	0324
T	Present work	7.301	14.172	23.888	37.301	53.536	74.825	98.193
	Roy [13]	7.382	14.844	25.300	37.924	53.664	73.444	98.372
	HF [2]	7.433	14.573	24.529	37.688	54.401	74.810	99.410

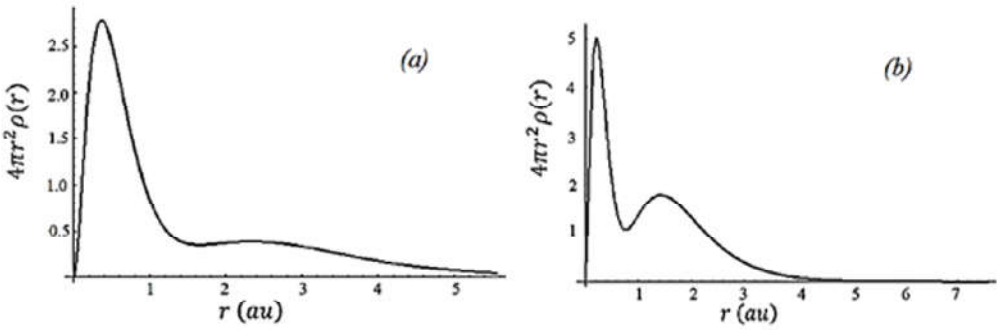

FIG. 1: Radial density plot of (a) Li and (b) B (by unit of au.).

It is satisfying that the CWDVR approach can be used to perform high precision calculation of the Kohn – Sham type equation with the use of only a few of grid points. Analyses of the results for exchange and correlation energies are given in the same table separately. The results from exchange energies (E_x)

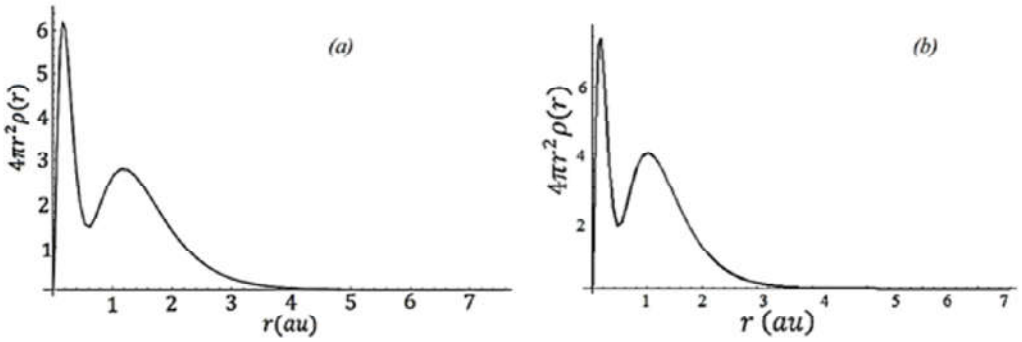

FIG. 2: Radial density plot of (a) C and (b) N (by unit of $au.$).

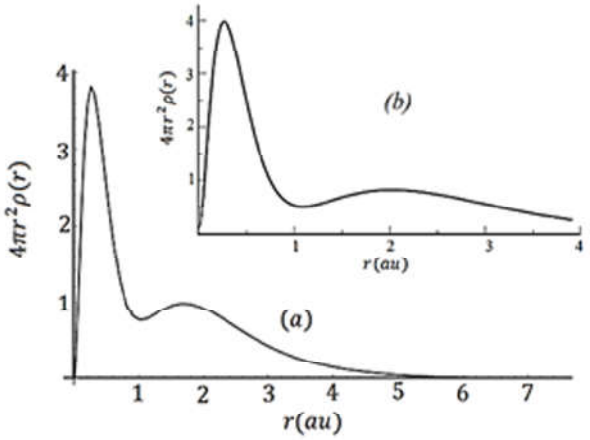

FIG. 3: Radial density plot of Be (by unit of $au.$).

calculations of the present calculations show a good agreement with the HF results [2]. For the Li, Be, B, C and F atoms, the calculated exchange energy is nearly exact, while for N, O and F there is an underestimation about 1.1%. This indicates that the simple local exchange functional in Eq.(5) is well accurate, compare to those of Amlan J Roy [14]. The "exact" correlation energies are considered for theLi, Be, B, C, N, O and F atoms in the Table I due to the comparison with other results. The Wigner – type correlation energy functional is likely seem to be sufficiently enough for the systems considered. For the Be atom, it is nearly exact, otherwise underestimated by about $5.1-12.5\%$; the Li atom is being the worst case. Compared with other generalized – gradient approximations (GGA), Perdew's GGA [15] correlation energy functional gives better results for Be, B and C but worse results for Li, N, O and F. We note that the primary purpose of this work is to explore the feasibility of extending the CWDVR to the solution of the Kohn – Sham type differential equation with imaginary time propagation. The LDA – type E_{xc} energy functionals can be easily adopted in the present CWDVR approach. Table I shows that the Viral theorem is nearly satisfied for Li, Be, B and C atoms. The calculated kinetic energy term for the Li atom is reasonably exact to HF, while for rest atoms there is an underestimation by $2.1-4.3\%$. In Figures 1 and 2, the radial density plots for lithium, boroncarbon and nitrogen are presented, where HF plot is not shown. In Figure 3, we report the radial density plots for beryllium. The inset (a) reports the result from present calculation; the inset (b) shows the HF plot for comparison. Here, the radial density plot shape from our calculation is in good agreement with

the HF plot.

IV. CONCLUSIONS

In conclusion, we present that the nonrelativistic ground state properties of Li, Be, B, C, N, O and F atoms can be calculated by means of time – dependent Kohn – Sham equations and an imaginary time evolution methods. The CWDVR approach shown to be an efficient and precise solution of ground – state energies of atoms. The calculated electronic energies are in good agreement with the HF values and are significantly better than the results in the other literatures. The approach is likely opens a road to solution of ionization and excitation states of many electron atoms.

Acknowledgments

This work was supported by the PROF2017 – 1895 at the National University of Mongolia.

[1] P. Hohenberg and W. Kohn, Phys. Rev. **136**, B864 (1964).

[2] R. G. Parr and W. Yang, Density – Functional Theory of Atoms and Molecules, Oxford Univ. Press, New York, (1989).

[3] Liang – You Peng and Anthony F. Starace, J. Chem. Physics **125**, 154311 (2006).

[4] D. Naranchimeg, L. Khenmedekh, G. Munkhsaikhan and N. Tsogbadrakh, Mongolian Journal of Physics, **3**, 55 (2017); arXiv:1810.01085 (2018).

[5] D. O. Harris, G. G. Engerholm, and W. D. Gwinn, J. Chem. Phys. **43**,1515 (1965).

[6] A. S. Dickinson and P. R. Certain, J. Chem. Phys. **49**, 4209 (1968).

[7] J. V. Lill, G. A. Parker, and J. C. Light, Chem. Phys. Lett. **89**, 483 (1982); R. W. Heather and J. C. Light, J. Chem. Phys. **79**, 147 (1983).

[8] C. Light, I. P. Hamilton, and J. V. Lill, J. Chem. Phys. **82**, 1400 (1985).

[9] D. Baye and P. H. Heenen, J. Phys. A **19**, 2041 (1986); V. Szalay, J. Chem. Phys. **99**, 1978 (1993).

[10] G. Machtoub and C. Zhang, Int. J. Theor. Phys. **41**, 293 (2002).

[11] K. M. Dunseath, J. M. Launay, M. Terao-Dunseath, and L. Mouret, J.Phys. **B35**, 3539 (2002).

[12] B. M. Deb and P. K. Chattaraj, Phys. Rev. A **39**, 1696 (1989).

[13] Amlan K Roy and Shih – I Chu, J. Phys. B: At. Mol. Opt. Phys.**35**,2075 (2002).

[14] Amlan K Roy, J. Math Chem. **49**, 1687 (2011).

[15] J. P. Perdew, Phys.Rev.B **33**, 8822 (1986).

Some results of quenched SU(3) flux tube using Wilson flow method

Battogtokh Purew[a], Sodbileg Chagdaa[a], Olaf Kaczmarek[b] and Enkhtuya Galsandorj[a]

[a] *Institute of Physics and Technology, Ulaanbaatar 13330, MONGOLIA and*

[b] *Physics Department, Bielefeld University, GERMANY*

In this work, we have studied error reducing property of the gradient flow method. For that reason, we have firstly calculated the flowed configurations of the quenched SU(3) gauge field at different values of flow time t including $0.01, 0.03$ and 0.05. The flux tube distributions are measured on lattice of volume $32^3 \times 8$ with the different $q\overline{q}$ separation distances, $R = 4a, 6a$, and $8a$ at fixed temperature $T/T_c = 1.29$. The results present that at the increasing flow time, the signal becomes much better, but important pieces of information are lost, because of the smearing effects of the Wilson flow.

I. INTRODUCTION

The gradient flow is a useful new technique for the study of gauge theories [1] and [2]. By introducing flow time coordinate t, the flow equation of the SU(3) gauge field is defined by following equation

$$\dot{B}_\mu(x,t) = D_\nu G_{\nu\mu}, \quad D_\mu = \partial_\mu + [B_\mu(x,t), \cdot] \quad , \tag{1}$$

where the dot denotes a derivative of t and $G_{\nu\mu}$ is field strength tensor on the gauge field. Without flow time, the gauge field $B_\mu(x,t)$ is equal to fundamental gauge field $A_\mu(x)$. The flow equation of the field is proportional to the gradient of the action [4],

$$D_\nu G_{\nu\mu}(x,t) \sim \frac{\delta S_G[B_\mu]}{\delta B_\mu} \tag{2}$$

gauge fields along the flow become smoother. It means the flow eventually reaches local minima of the Yang Mills action, which is quite useful when studying the topology of the gauge field. In this case, the smearing radius can be obtained by considering leading order perturbation theory in the bare coupling g. The smearing radius is then $r_{smear} = \sqrt{8t}$

In this work, we trying to explore its error reducing properties. Correlation functions made of this smoothed fields turned out to have a well defined continuum limit [1]. Furthermore, the flow suppresses the ultraviolet contributions of correlation functions at distances $r_{smear} \gtrsim \tau$ or frequencies $\pi/r_{smear} \gtrsim \omega$, by reducing the spectral weight in the spectral representation of the correlator.

The gauge theories are affected by fluctuations at the scale of the ultraviolet (UV) cutoff. As a consequence, observables which are measured on the lattice suffer on these short distance fluctuations. Wilson flow method is amongst others of a smoothing procedure such as cooling, smearing procedures which can filter out ultraviolet (UV) fluctuations. This method is governed by a differential equation which means that we have a better analytical control of the smoothing procedure

In terms of the flow link variables $U_t(x,\mu)$, the lattice formulation of the flow is given by the equations [5]

$$\dot{U}_t(x,\mu) = -g_0^2\{\partial_{x,\mu}S_W(U_t)\}U_t(x,\mu), \quad U_t(x,\mu)|_{t=0} = U(x,\mu) \tag{3}$$

in which $\partial_{x,\mu}$ is a $su(3)$ Lie-Algebra valued differential operator. We choose S_W to be the standart Wilson gauge action given by equation

$$S_W(U) = 1/g_0^2 \sum_p ReTr\{1 - U(x,\mu)\} \quad . \tag{4}$$

Therefore, the gradient flow also known as Wilson flow.

To compute these variables numerically as first we define the SU(3) valued differential operator acting on function $f(U)$

$$\partial^a_{x,\rho} f(U) = \frac{d}{dt} f(U_t)|_{t=0}, \quad U_t(y,\sigma) = \begin{cases} e^{tT^a}U(x,\rho), & \text{if } (y,\sigma) = (x,\rho) \\ U(y,\sigma), & \text{otherwise} \end{cases} \tag{5}$$

where T^a are the SU(3) generators. Then inserting the definition of the plaquette and make use of the product rule e.g. few step later the terms of Wilson flow equation becomes more compact

$$\begin{array}{ll} \partial_{x,\rho}S_W(U_t) & = \frac{1}{2g_0^2}(\Omega(x,\rho) - \Omega^\dagger(x,\rho)) - \frac{1}{6g_0^2}Tr(\Omega(x,\rho) - \Omega^\dagger(x,\rho)) \\ \Omega(x,\rho) = U(x,\rho)W^\dagger(x,\rho) & \end{array} \tag{6}$$

where $W^\dagger(x,\rho)$ is a definition of staple. This formulation of flow equation can be easily constructed from link variables on the lattice and solved numerically.

The existence, uniqueness and smoothness of the Wilson flow at all positive and negative times t is rigorously guaranteed on a finite lattice. Moreover, from eq.6 one immediately concludes that the action $S_W(U_t)$ is a monotonically decreasing function of t. The flow therefore tends to have a smoothing effect on the field and it is, in fact, generated by infinitesimal stout link smearing steps [3]. It means we can reduce UV fluctuations of the lattice field configuration.

II. NUMERICAL DETAILS

The lattice form of the field equation at last became first order differential equation as follows

$$\begin{array}{ll} \frac{d}{dt}U_t(x,\mu) & = -\frac{1}{2}\Omega(x,\mu) - \Omega^\dagger(x,\mu) - \frac{1}{6}tr(\Omega(x,\mu) - \Omega^\dagger(x,\mu)]U_t(x,\mu) \\ \frac{d}{dt}U_t(x,\mu) & = f(U)U_t(x,\mu) \end{array} \quad . \tag{7}$$

Now we have to solve the equation using a numerical method. Therefore, we choose Runge-Kutta method amongst others of another solvers. The purpose of this section is to introduce the numerical and algorithmic

concepts which we have used in our program. Wilson flow a numerical integration has to be considered which acts on SU(3) matrices. Such a method is described in the first part of this section. Subsequently, we describe in the second section, how we implement the Wilson flow using the Runge-Kutta method.

A. Runge Kutta

Numerical methods for ordinary differential equations approximate solutions to initial value problems of the form,

$$y`(t) = F(t, y(t)), \quad y(t_0) = y_0, \quad y : \Re \to \Re^d \tag{8}$$

where $y(t)$ is a exact solution. Since it is in general not possible to obtain the exact solution, an approximation y_n at different discrete points t_n is used. The S-step Runge Kutta method is a single-step method, which solves such equations as written in table,

for $r = 1 : S$ do
$T_r = hc_r + t_n$
$Y_r = \sum_{k=1}^{S} a_{rk} F_k + y_n$
$F_r = hF(T_r, Y_r)$
end
$y(n+1) = \sum_{k=1}^{S} b_k F_k + y_n$

where h is the step size between consecutive points t_n and t_{n+1}. The coefficients a_{rk} and c_r define the respective method and can be interpreted as weights of the numerical quadrature for the integral

$$\int_{t_n}^{t_{n+1}} F(t, y(t))dt$$

The quantities F_k can be seen as intermediate steps between t_n and $t_n + 1$. The general Runge-Kutta is implicit, which means that to get F_k , it is necessary to solve a system of non-linear equations. If $a_r k = 0$ for $r \geq k$, then the Runge-Kutta is explicit.

In this case we need to solve differential equations, which are defined on Lie groups. To be more precise, we want to solve equations of type

$$F(y) = \dot{y} = A(y)y, \quad y \in G, \quad A(y) \in g \tag{9}$$

where G is a Lie group and g Lie algebra. We cannot simply apply (8) on (9), because even if $y \in G$ and zG an update of the form $y + hA(z)z$ is not an element of the Lie group. Thus we apply Grouch-Grossman method which replaces the update operation in $hA(z)z$ with $exp(hA(z))y$. Now three step Runge Kutte algorithm become as table,

for $r = 1 : S$ do

$Y_r = exp(\sum_k \alpha^k_{rJ} F_k)...exp(\sum_k \alpha^k_{r1} F_k)(y_n)$

$F_r = hF_{Y_r} = hA(Y_r)$

end

$y_{n+1} = exp(\sum_k \beta^k_{rJ} F_k)...exp(\sum_k \beta^k_{r1} F_k) y_n$.

where $a^k_r = \sum_{j=1}^J \alpha^k_{rj}$ and $b^k = \sum_{j=1}^J \beta^k_j$. If we consider now the special case, when the Lie group is equal to the linear space. Exponentials can be rewritten as $exp(hF_p)y_n = y_n + hF_p$. In this case algorithm becomes the standard Runge-Kutta method,

$$Y_r = y_n + h\sum_{k=1}^{S} a^k_r F_k, \quad r = 1, ..., S, \qquad y_{n+1} = y_n + h\sum_{k=1}^{S} b^k F_k.$$

Martin Luscher calculated the coefficients for the explicit 3-step Runge-Kutta in [1]. Which is shown in the next equations

$$\begin{aligned} Y_0 &= y_n \\ Y_1 &= exp(1/4F_0)Y_0 \\ Y_2 &= exp(8/9F_1 - 17/36F_0)Y_1 \\ y_{n+\epsilon} &exp(3/4F_2 - 8/9F_1 + 17/36F_0)Y_2 \\ F_i &= \epsilon A(Y_i) \end{aligned}$$

where ϵ is the updating step size. This integration scheme is accurate up to errors of order ϵ^4, while the total error of the integration scales like ϵ^3.

B. Technical setup

Computing the Wilson flow is very time consuming. We reduce the computational time by parallelizing the code. The lattice can be domain decomposed into sub lattices equal to the number of parallel processes. Then, the smearing operations are done on each sub-lattice in parallel. After that we need to implement the 3rd Runge-Kutta scheme. For this purpose we allocated two gauge fields. The first gauge field holds the field which will be smeared, while the second one is used as a temporary field which stores the results of the exponents in Runge-Kutta algorithm. The Runge-Kutta algorithm is implemented as follows:

1. Compute F_0 by using the link variables from the first gauge field and store the results in the second gauge field.
2. Compute Y_1 with the previously calculated F_0 and store the results in gauge field one.
3. Exchange halos which is each process allocates additional memory space.
4. Compute $9/8F_1 - 17/36F_0$ by using gauge field one and two and store the results in gauge field two.

5. Compute Y_2 with the exponents stored in gauge field two and store the results in gauge field one.

6. Exchange halos.

7. Compute the final smeared field $y_{n+\epsilon}$ by using gauge field one and two and store the result in gauge field one.

This algorithm is then applied multiple times on the gauge field until the desired flow time is reached ($t = n\epsilon$).

III. PROGRAMMING

In this work we have used two separated program. First one is our own GPU code which is measure flux tube distribution. Second one is implemented in Bielefeld University, it is named ParallelGPUCode. It can compute flowed configuration using previously generated configurations. In this section we are talking about these programs.

A. Our GPU code

We changed our previous SU(2) program into more accurate program that is based on SU(3) lattice gauge theory. Firstly, we have changed mathematical operations such as a addition, subtraction, multiplication, division that are defined between 2×2 matrices, real numbers and complex numbers into operations between the 3×3 matrices and the numbers. Then we generated configurations using the pseudo-heatbath and Overrelaxation algorithms as already mentioned in our previous work [6]. Basic instruction of the code is shown in figure 1.

B. Parallel GPU code

The Wilson flow algorithm was implemented into the ParallelGPUCode. It is a great framework which offers many basic functions for Lattice QCD applications. This includes a lattice structure which can be domain decomposed into sub-lattices for parallel processing as well as the necessary halo functionality. The communication interface and the reading and writing routines are based on the Messaging Passing Interface (MPI). Furthermore, this framework offers basic SU(3) functions, which are frequently used in the program. The Wilson flow algorithm was implemented as described in [2] more precisely.

IV. RESULTS

In this work, we studied noise reducing property of the Wilson flow. In order to do that we show some results of the Wilson flow on quenched configurations. Therefore we firstly generated configurations using the Heat Bath and Overrelaxation algorithms as already mentioned in [6]. One sweep consists of one Heat Bath

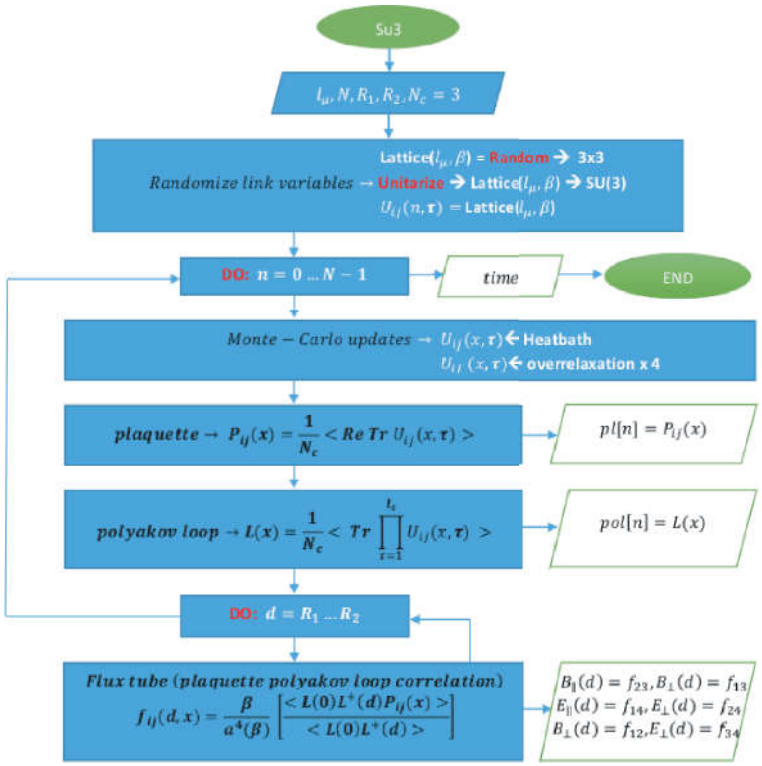

FIG. 1: Algorithmic scheme of the our SU(3) program.

and four Over-relaxation steps. Then we computed flowed configurations using these quenched configurations. At last, we measure some observables including plaquette, Polyakov and flux tube distributions.

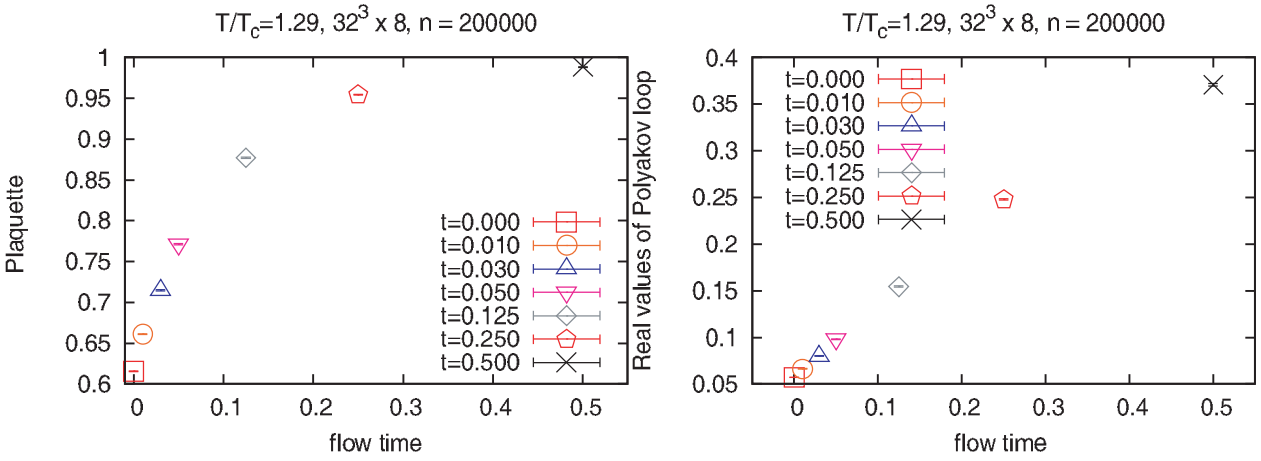

FIG. 2: Flow time dependence of the expectation values of the plaquette (left) and the expectation values of the Polyakov loop (right).

Before seeing the results, We have checked the program. According to check the program, we measured plaquette and Polyakov loop operators using our new program and the main code in Bielefeld, ParallelLatticeCode, then compared these results. In figure 2, we present the plaquette and Polyakov loops expectation values, which are measured in $32^3 \times 8$ with the temperature $T/T_c = 1.29$ against the flow time $t = 0.01 - 0.5$

in lattice unit. Our measured operators are almost equal to the ParallelLatticeCode's results. Nevertheless, there is a little bit difference exist with all the values of the operators. The difference only exists after the 5th digit, because of the precision type. It can say that our program works properly.

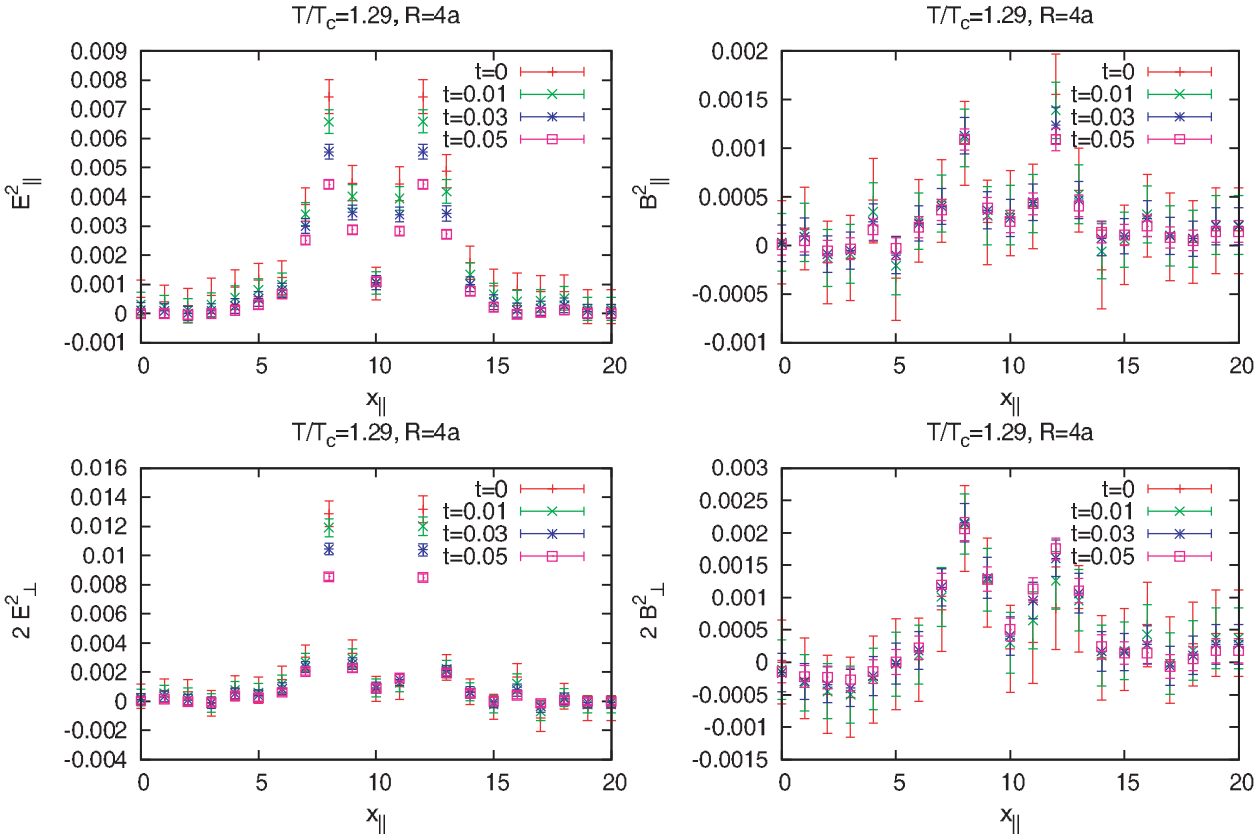

FIG. 3: Flux tube distribution of the quark anti-quark pair.

The next step, we computed flux tube distribution at three different flow time, $t = 0.01, 0.03, 0.05$. These results and flux tube distribution without Wilson flow are plotted in figure 3. First two plots show the parallel distribution and next two plots present the transverse distribution of the chromo-electric and chromo-magnetic field. From the figure, we can see that the signal became much better with the increasing flow time. Also, one can shows that each component of the field's value decreased with the increasing flow time.

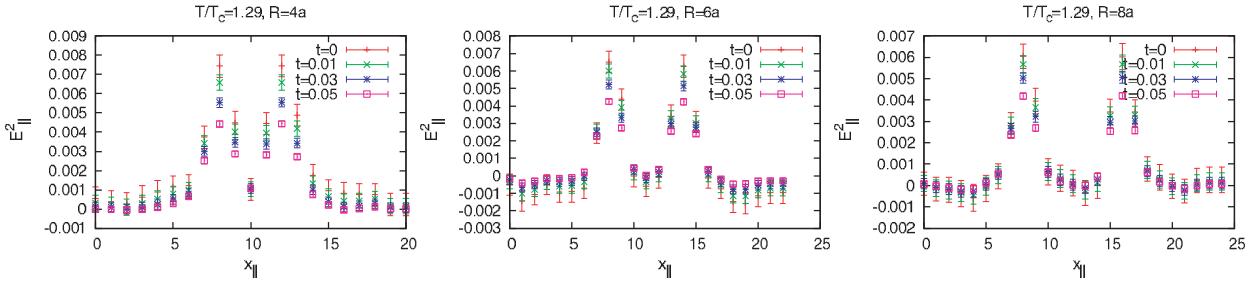

FIG. 4: The parallel chromo-electric field distribution at different quark antiquark seperation distances

Finally, we tried to explore dependence between quark-antiquark separation distance and flow time in flux tube distribution. Figure 4 include three plots which are plotted in different separation distances, $R = 4a, 6a,$

and $8a$. Each plot shows the parallel chromo-electric component of the flux tube at the four different values of the flow time, as a function of a vertical component of space. From the figure, we can not find the dependence. In another word, the Wilson flow method works fine all the separation distances.

V. CONCLUSION

Using a Wilson flow method, we have implemented a new technique to increase signal-noise-ratio for our program. This technique works as follows:

- generate configuration using our code,
- compute flowed configuration by the ParallelGPUCode,
- measured corresponding operators such as the expectation value of plaquatte, the Polyakov loop and flux distribution, using our code.

The configurations are computed directly for flow time, $t = 0.01, 0.03$ and 0.05. Then we measured the operators for each configuration on lattice of volume $32^3 \times 8$ with the different $q\overline{q}$ separation distances $R = 4a, 6a$, and $8a$ at fixed temperature $T/T_c = 1.29$. The expectation values showed the technique gives us accurate results. Therefore we can use it in our research. After that, we measured flux tube distribution using the flowed configurations. The plots show that if we increase flow time, the signal-nose-ratio increase linearly, but we lose much information too. For that reason, we have to choose flow time very carefully.

VI. ACKNOWLEDGEMENTS

We would like to thank colleagues of Faculty of Physics, University of Bielefeld for their friendly and generous cooperation.

---

[1] M. Luscher. Properties and uses of the Wilson flow in lattice QCD. In: Journalof High Energy Physics 8, 71 (Aug. 2010), p. 71.

[2] Lukas Mazur, "Applications of the Gradient Flow method in Lattice QCD". Master dissertation, 2017.

[3] C. Morningstar, M. Peardon, Analytic smearing of SU(3) link variables in lattice QCD, Phys. Rev. D69 (2004) 054501

[4] A. Ramos. The gradient flow in a twisted box. In: PoS Lattice2013 (2014), p. 053. arXiv: 1308.4558 [hep-lat].

[5] M. Luscher. Trivializing Maps, the Wilson Flow and the HMC Algorithm. In: Communications in Mathematical Physics 293 (Feb. 2010), p. 899.

[6] Ch. Sodbileg, P. Battogtokh, G. Enkhtuya, Results of programming static meson system in SU(3) lattice gauge theory, submitted into Journal of Mongolian Physical Society, 2017.

Quantum states of InGaAs/InAlAs quantum well detector for broad-range photon detection

O. Oyun-Erdene[1], G. Biasiol[2], and G. Tamiraa[1]

[1]*SEAS, National University of Mongolia, Ulaanbaatar 14200, Mongolia and*

[2]*CNR-IOM, TASC Laboratory, Area Science Park, Trieste 34100, Italy*

The InGaAs/InAlAs quantum well (QW) heterostructures, including single quantum well, superlattices have special advantages for applications in high speed electronic and photonic devices. Their direct, low energy band gap and high electron mobility renders it capable of detecting photons ranging from visible to X-ray at room temperature. In this work, we simulated properties of quantum states inside the quantum well with different width thickness (5-45 nm). The simulation shows, a number of states changes from 1 to 6 while the well width increasing. The electron concentration was increasing until 25 nm then started slowly stabilizing.

Keywords: InGaAs/InAlAs quantum well, X-ray detector

I. INTRODUCTION

In last decades, semiconductor quantum wells (QW)s have attracted to growing interest for laser applications, photon detection due to their potential of increasing gain by confinements. Quantum confinements of carriers in the QWs leads to quantized subband energies. InGaAs/InAsAs QW heterostructures on indium phosphide (InP) substrates are used as material for field-effect high-electron-mobility transistors (HEMTs) in ultrahigh-frequency electronics operating in the multimeter wavelength region [1, 2]. Recently, the possibility to use QW photon detectors in X-ray regions reported as a position sensetive broad-band X-ray detector based on InGaAs/InAlAs QWs growing on gallium arsenide (GaAs) substrate [3–5]. Due to its direct low energy band gap and high electron mobility, quantum well (QW) devices based on arsenide semiconductors have been proposed as fast efficient sensors from visible light to hard X-rays. Such QW devices consist of atomically controlled semiconductor layers epitiaxilly grown on semi-insulating GaAs substrates by techniques such as Molecular Beam Epitaxy (MBE) [6, 7]. Two-Dimensional Electron Gases (2DEG) forming inside QW with high In concentration x offers potential advantages for device applications. In particular, achievement of 2DEG in metamorphic, almost unstrained InGaAs/InAlAs QW can be obtained by inserting 'virtual substrates' of InAlAs buffers with graded In composition grown on a GaAs substrate [4, 8]. 2DEG features very high carrier mobility and population of electrons inside the well. However, quantum states of the electron in the QW is not deeply studied. In this work, numerical simulations on the device were performed by 1D Poisson Schroedinger solver to calculate wavefunctions (WF), its eigenvalues (energy levels), carrier concentrations etc. To confirm optimal growth condition, a width of the QW has been changed from 5 nm to 45 nm. Furthermore, eigenvalues and probability apmlitude of each WFs were explored in terms of QWs width. It was confirmed that 25 nm is optimal thickness of the QW region due to the saturation of the electron concentration and the number of states.

II. DEVICE FEATURE AND SIMULATION DETAIL

Metamorphic, modulation InGaAs/InAlAs QW samples were grown by MBE on GaAs 500 μm semi-insulating wafers. Fig. 1 shows the layered structure of the device. In order to block impurities from the bulk GaAs substrate, an AlGaAs/GaAs superlattice was grown after 200 nm of GaAs substrate. Another 200-nm-thick GaAs layer was introduced before an InAlAs step-graded Buffer layer (BL) with x increasing from 0.15 to 0.75. This allows the lattice constant to be tuned in order to reduce the residual strain due to the lattice mismatch [9]. Then a 25-nm-thick InGaAs QW containing a 2DEG was placed between 50-nm-thick InAlAs barrier layers. The charge density and carrier mobility in the QW were characterized at room temperature resulting in an electron concentration of 7.7x10^{11}cm^{-2} and a mobility of 1.1x10^{4} cm^{2} V^{-1} s^{-1}.

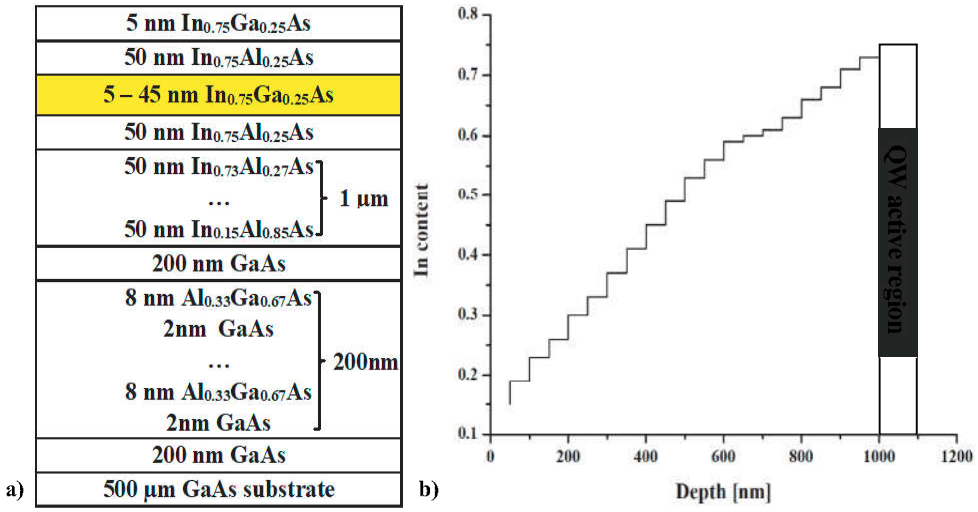

FIG. 1: a) Layout structure of the wafer, b) In content in the step-graded buffer layer of InGaAs/InAlAs QW

Simulations on devices are a critical procedure for the design and optimisation of novel semiconductor devices. In the QW device containing 2DEG near to the surface, effects of surface state in heterostructure is more presented and depleting the electron density in the QW and modifying the optical and electron-transport properties. To simulate the influence of the QW widths, several width ranging from 5nm to 45nm was considered in the simulation using 1D Poisson Schrodinger solver [10]. Some missing materials such as InGaAs, InAlAs in the solver package were added to the core file. An important issue in any device simulation is the inclusion of correct material parameters such as band offset, carrier mobility, effective mass etc. In our simulation band offset, electron and hole effective masses added as function of material composition and electron carrier mobility was chosen from experimental measurements for the InGaAs. The simulation considered the exact layered structure of the QW devices grown in the MBE. All the calculation performed at room temperature (300 K).

III. RESULT AND DISCUSSION

The calculated band structures with two different QW width (5nm and 40nm) are shown Fig. 2. As the chemical composition of the BLs changes, a staircase band structure is shown by the simulation, followed by the QW region. Number of quantum states inside the QW increases in terms of the width [Fig. 3a]. Wider well has more population of electrons, which are occupying more number of states.

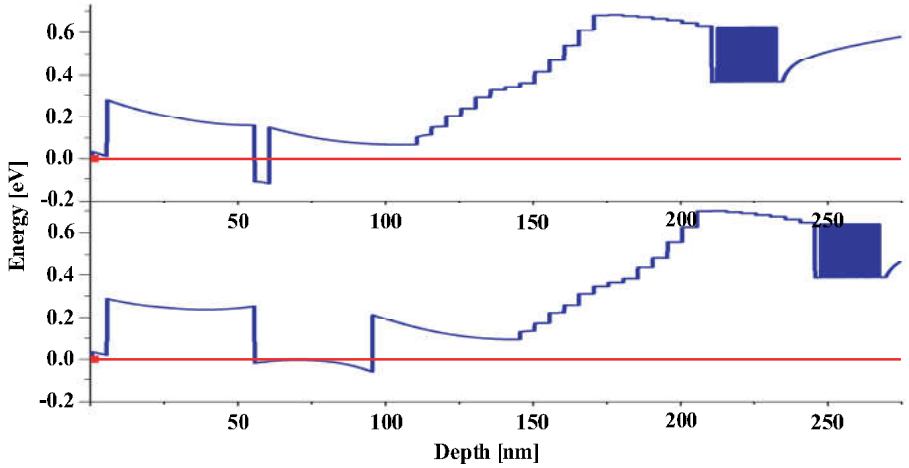

FIG. 2: Calculated band structures with width QW 5 and 40 nm. The graded staircase Buffer layer and Super lattice are clearly shown.

Furthermore, a probability amplitudes of the ground states are shown in Fig. 3b with different QW region thicknesses. The probability amplitude is more symmetric in narrow wells than the wider ones. When the QW region is widening, the probability amplitute is shifting to the bulk side and becoming non symmetric due to the effect that the bulk is supporting more electrons than the surface.

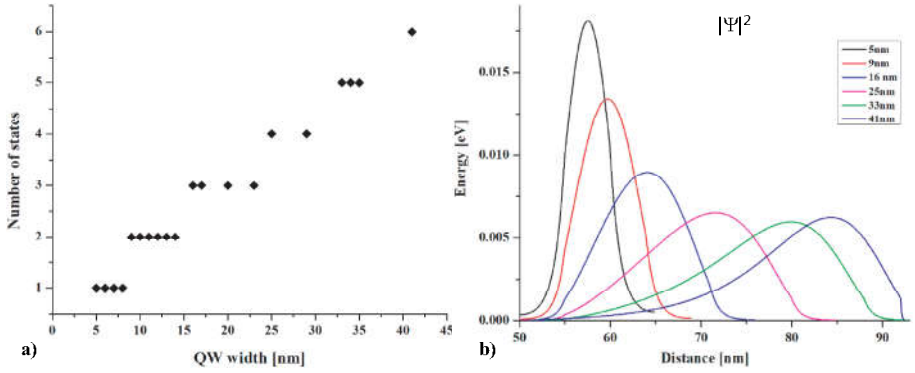

FIG. 3: a) The probability density of electron for the ground state, b) Number of states changes in different width QW.

Moreover, only ground state was found while the QW width is up to 8nm, then second quantum states are identified from 9nm-15nm wide wells. We found 6 eigenfunctions by solving Schrodinger equations in case of 45nm-wide-well Fig.3b and each wavefunctions are illustrated inside the QW [Fig.4]. The wider QWs have more states due to the more electron injection from the substrate. The basic wave functions of a rectangular

quantum well were observed from the simulation.

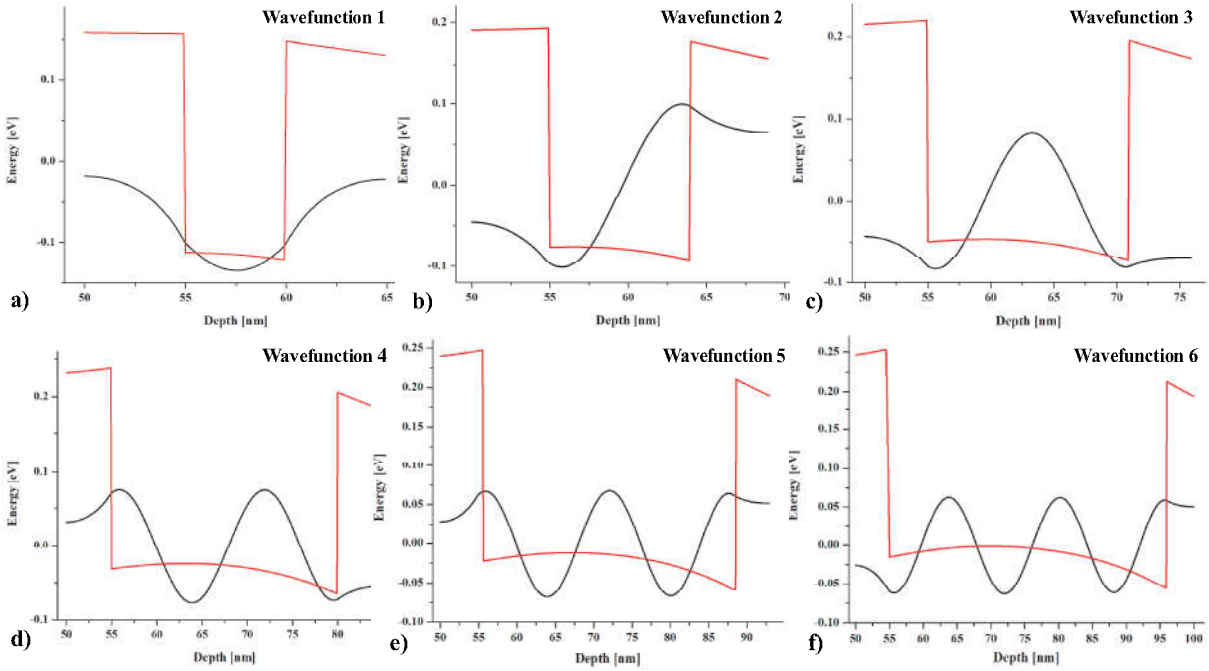

FIG. 4: Six wavefunctions (WF) are shown above. The functions are symmetric inside the QW.

Because of the difference in QW region thickness, an increase in the electron concentration arises as well. Presence of only ground state shows a decrease in the energy values while the QW region is widening until second and third quantum states appear. In case of 16nm-wide-QW, the electrons are filling the ground state then other two states are occupied due to its higher population, which makes energy of the ground state arises. Other eigenvalues of the WFs are decreasing while the QWs is broadening [Fig.5]. We observed significant arise on the electron concentration up to the width value of 20nm, then the population number is stabilized. Wider wells lead to have more electrons, however, the QW is fully occupied by the electrons at the certain thickness of the well. For the growth condition, 25nm of active region thickness was chosen to be the optimal value.

IV. CONCLUSIONS

We calculated the band structures of the QW devices with different QW widths. The probability amplitude of the carrier is shifted to the bulk side and becoming non symmetric in the wider wells due to the more electron injection from the bulk substrate. When the thickness of the QW is widening, more electrons are injected to the well causing the increase on the number of states. However, we observed certain plateau on the electron concentration started from 20nm-wide-well. Furthermore, the number of electrons supported from the bulk is becoming constant, the energy of the WFs are decreasing in wider wells. In the end, 25nm of active region thickness was confirmed as optimal QW width.

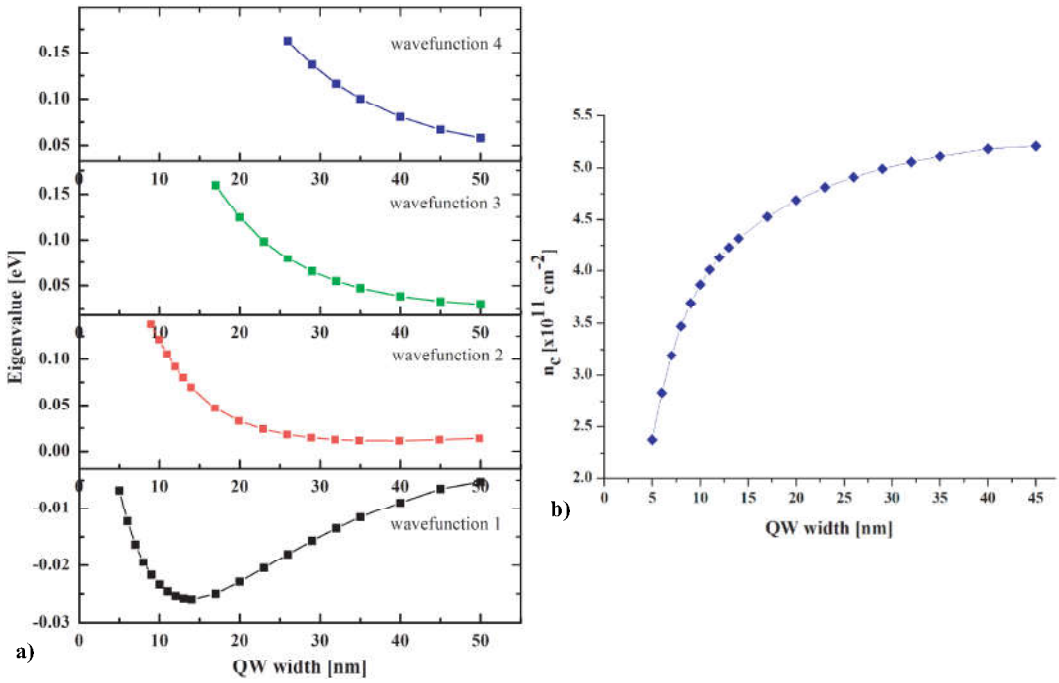

FIG. 5: a) Eiginvalue for different width QW, b) electron concentration of QW.

Acknowledgments

This work is supported by Asian Research Center Project P2017-1322 .

[1] E. Y. Chang et al., Appl. Phys. Express 6, 034001, (2016)

[2] J. A. del Alamo, Nature 479, 317, (2011)

[3] M. Antonelli et al., Fast board-brand photon detector based on quantum well devices and charge-integrating electronics for non-invasive FEL monitoring, AIP Conference Proceedings 1741, 030001 (2016)

[4] S. Adachi et al., Properties of Semiconductors Alloys: Group-IV, III-IV and II-VI Semiconductors (Wiley, New York, 2009)

[5] T. Ganbold et al., Fast, multi-wavelength, efficiency-enhanced pixelated devices based on InGaAs/InAlAs quantum wells, J. Inst., 10, C03009 (2015)

[6] T. Ganbold et al., Photon-sensitive multi-wavelength photon detectors based on epitaxial InGaAs/InAlAs quantum wells, J. Cryst. Growth 425, 341-345 (2015)

[7] T. Ganbold et al., Position sensitive photon detectors using epitaxial InGaAs/InAlAs quantum wells, J. Inst., 9, C12043 (2014)

[8] F. Capotondi et al., Strain induced effects on the transport properties of metamorphic InAlAs/InGaAs quantum wells, Thin Sol. Films, 484, 400-407, (2005

[9] F. Capotondi et al., Two-dimensional electron gas formation in undoped In0.75Ga0.25 As/In0.75Al0.25As quantum wells, J. Vac. Sci. Technol., B22 (2004)

[10] G. Snider, 1D Poisson, http://www.nd.edu./ gsnider/.

Effect of Hot-wire Temperature on Properties of Si-rich Silicon Nitride Thin Films

Yan, Zefei, Ding Desong, Zhou Bingqing* , Bu Xinxin, Siqin Bater

Key Laboratory of Physics and Chemistry for Functional Material, College of Physics and Electron Information,Inner Mongolia Normal University,Huhhot 010022, China

Abstract：As keeping other deposition parameters constant, by changing the hot wire temperature, Si-rich silicon nitride thin films were prepared by hot wire chemical vapor deposition method using SiH_4, NH_3 and H_2 as reaction gas source. The optical band gap, crystalline phase, chemical bond types and other related information were characterized by fluorescence spectra (PL), ultraviolet-visible (Uv-Vis) light transmittance spectra, Fourier transform infrared absorption spectra (FTIR). The results show that, with increasing of the hot wire temperature, the fracture of the N-H bonds and Si-H bonds reduces the bond density of the Si-H, N-H bond. A larger number of hydrogen atoms overflow the thin film, making the Si and N dangling bonds cannot be passivated, which cause the Si-N bonds to recombine again. The stability and compactness of the films were improved by increasing the Si-N bond density. However, with increasing of the hot wire temperature, the reduction of hydrogen content leads to a significant decrease of hydrogen desorption effect and the increase of the defect state density, widening the band gap, decreasing the order of the films. At the moment the films show a Si-rich state. As the hot wire temperature increases further, the Si and N in the films can fully relax, which is favorable for the formation of the Si-Si bond. The accumulation of many Si-Si bonds leads to the formation of the silicon cluster nanoparticles. Therefore, the silicon quantum dot materials embedded in the silicon nitride matrix are prepared by hot wire chemical vapor deposition with a higher hot wire temperature without further annealing.

Key words: hot wire chemical vapor deposition, Si-rich silicon nitride film, hot wire temperature, silicon quantum dot, chemical bond

I. INTRODUCTION

Silicon-based solar cells are main form of commercial photovoltaic devices because of their rich materials, mature technology, and high stability[1]. As an anti-reflective film for solar cells, silicon nitride has excellent optical properties such as high resistivity, high chemical stability, high light transmittance, high hardness, good insulation, and wide range of refractive index changes [2]. At the meantime, silicon nitride films also have good passivation effect [3], good optical properties and widely applications in the microelectronics industry and solar cells. The silicon quantum dot (QD) materials embedded in silicon nitride matrix are usually prepared by magnetron sputtering or plasma-enhanced chemical vapor deposition, with post high temperature annealing. However, there are few reports on the preparation of silicon quantum dot thin film materials using hot wire chemical vapor deposition (HWCVD) technique. During the process of preparing the thin film materials by hot wire chemical vapor deposition method, the hot wire temperature can reach 1700°C or even higher. Not only a large number of Si-N bonds can be generated, but also Si-Si bonds can be directly formed.

Silicon quantum dots are also generated directly during the formation of silicon nitride, so as to avoid the high-temperature post annealing process. Therefore, it is of great significance to study the hot-wire preparation of silicon QD thin film materials embedded in silicon nitride matrix.

In this paper, high purity SiH_4, NH_3 and H_2 are used as reaction gas sources by changing the temperature of the hot wires to prepare silicon nitride thin films on glass and crystalline silicon substrates. The micro structure, chemical bond content, optical band gap and optical properties of the films were characterized by the UV-visible spectrophotometer, infrared absorption, and PL spectra.

II. EXPERIMENTAL DETAILS

The samples are prepared by hot wire chemical vapor deposition (HWCVD) technology keeping other deposition parameters constant, with changing hot wire temperature. The p-type crystal Si wafers (100) and Corning7059 type glass were used as the substrate. The hot wire is tungsten wire of 0.5mm diameter, and the four hot wires are arranged in parallel with distance of 300mm apart. The distance between the hot wire and the substrate is 550mm. The hot wire temperature is obtained by infrared detector. Using high purity SiH_4 (99.9999%), NH_3 (99.9999%) and H_2 (99.9999%) as reaction gas sources, the gas flow rates of SiH_4, NH_3 and H_2 are 1.0sccm, 15sccm, and 50sccm, respectively. The substrate temperature, the deposition pressure and the deposition time are 200℃, 20Pa and 30min, respectively. A series of samples were prepared by adjusting the hot-wire temperatures (1450°C, 1540°C, 1630°C, 1690°C, 1740°C) under the other deposition parameters constant. .

III. RESULTS AND DISCUSSIONS

3.1 Bonding properties of thin films

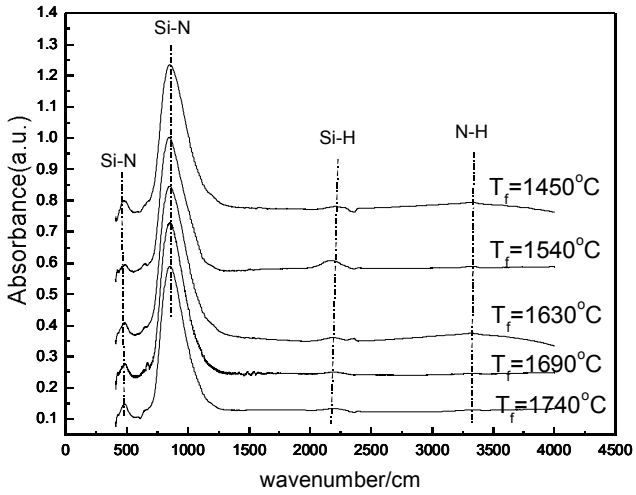

Fig. 1. FTIR spectra of the film samples at different hot wire temperatures

Figure1 shows FTIR spectra of the film samples at different hot wire temperatures. In figure 1, the absorption peak located around 485 cm^{-1} corresponds to the Si-N bond symmetric stretch vibration mode, and the absorption peak at around 839 cm^{-1} corresponds to the asymmetric stretch vibration mode of the Si-N bond. The absorption peak at near 2100cm^{-1}corresponds to the stretch vibration mode of the Si-H bond and the absorption peak near 3300cm^{-1} corresponds to the stretch

vibration mode of the N-H bond. All the above absorption peaks are consistent with the typical infrared absorption peaks of silicon nitride in the reference [4]. It can be seen from the fig.1 that absorption peak of the Si-H bond at around 2100 cm^{-1}has a blue shift. Lucovsky[5] thank that the reason of the blue shift is mainly due to the different electronegativity of H and N atoms in the silicon nitride films. The absorption peak at about 645cm^{-1} is the characteristic absorption peak of the Si-H bond bending vibration mode, and the change of the vibration strength was very small with increasing of the hot wire temperature. As the hot wire temperature increases, the intensity of the N-H and Si-H bonds gradually decreases until the peaks completely disappear beyond 1600°C. The reason is that the Si-H and N-H bonds are extremely fragile at high temperature, H atoms overflow the thin films, and the N and Si atoms are released for recombination. The above process can be explained by the chemical equation (1)[6].

$$Si\text{-}H+N\text{-}H \rightarrow Si\text{-}N+H_2. \quad (1)$$

The fracture of the Si-H bonds produces a large number of Si suspension bonds. The recombination of the Si suspension bonds and Si leads to the aggregation of Si crystal phase and promotes the growth of silicon cluster nanoparticles. In the infrared spectra, the absorption peak of the Si-Si bonds at 650cm^{-1} is enhanced with increasing of the hot wire temperature. When the N-H bonds break, the N atoms combine with the spare Si atoms to form the Si-N bonds, resulting in an increase of the Si-N bonds in the thin films. From the figure 1, we can see that the strength of the asymmetric stretch vibration absorption peak and the symmetric stretch absorption peak of the Si-N bond gradually increase with the increase of the hot wire temperature.

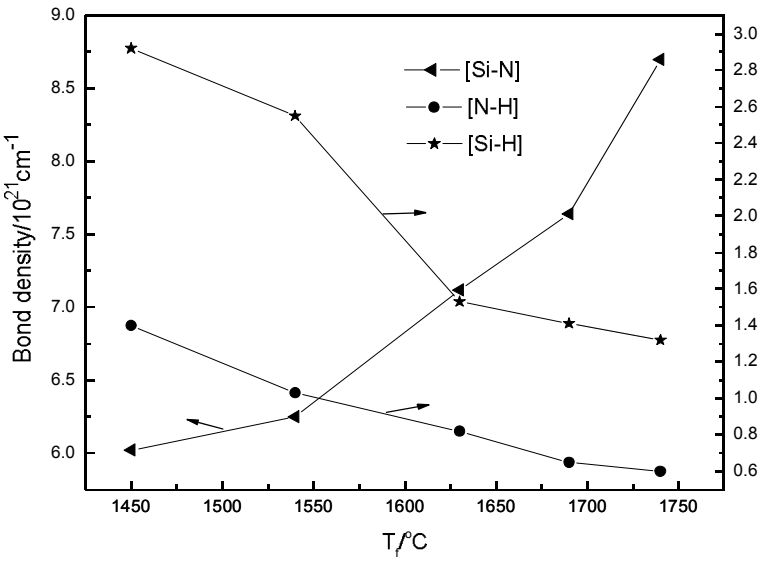

Fig. 2. Influence of hot wire temperature on the bond density

The density of bonds in the thin films was calculated by the method of Lanford and Rand[7,8]. The density C_x of the Si-H, Si-N, and N-H bond structures can be determined by formula (2)[9, 10, 11] .

$$C_x = A\int \frac{\alpha(\omega)}{\omega} d\omega . \qquad (2)$$

Where C_x is the bond density of Si-N, Si-H or N-H. X is a bonding mode. A is the correction factor. The $\alpha(\omega)$ is the absorption coefficient and ω is angular frequency. The bond density correction factors of the Si-N bond and the N-H bond are $6.3 \times 10^{18}cm^{-2}$ and $2.8 \times 10^{20}cm^{-2}$, respectively. The Si-H bond peak positions are diverse, and the Si-H bond peaks in the films are all at 2240 cm^{-1}, so the correction factor is 2.0×10^{20} cm^{-2}. Fig. 5-2 shows that the effect of different hot wire temperatures on the bond density. As shown in the figure, with the increase of the hot wire temperature, the Si-H bonds and the N-H bonds decrease monotonously. This is the opposite of the change in the Si-N bonds. As the temperature of the hot wire rises, the fracture of the Si-H and the N-H bonds reduces the density of the Si-H and N-H bonds and makes Si and N atoms recombine again to form the the SI-N bonds. The density of the Si-N bond increases, and both stability and compactness of the samples were improved.

3.2 UV-visible spectra analysis

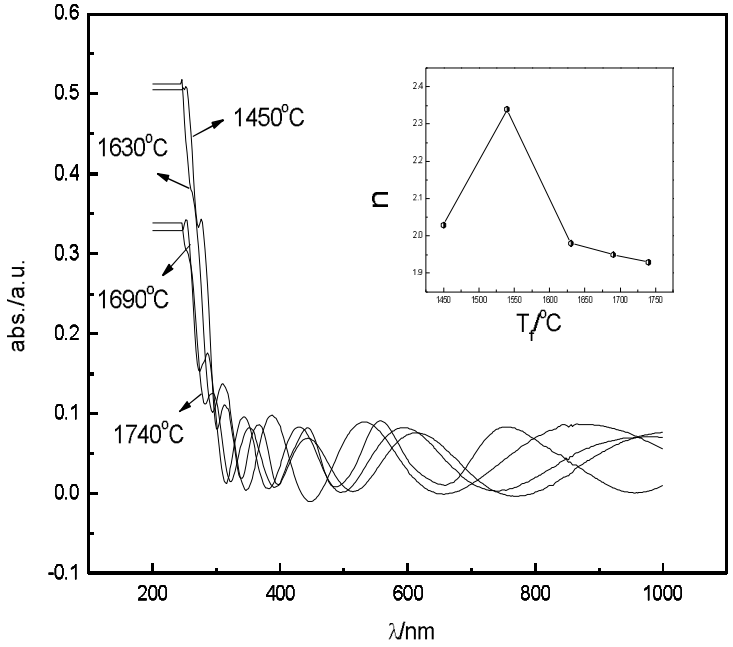

Fig.3. UV-Visible absorption spectra with different hot-wire temperatures
(the illustration is the refractive index change with the temperature)

Figure 3 shows the UV-Visible absorption spectra of samples prepared at different hot wire temperatures. As shown in the inset of Figure 3, with the increase of the hot wire temperature, the refractive index n of the samples increases firstly and then decreases, and the refractive index n is around 2.0. In order to further understand the optical characteristics of the films, the optical band gap Eg and Urbach Energy E_U are also calculated. Optical band gap E_g is calculated by Tauc formula[12]:

$$(\alpha h\upsilon)^{1/2} = B(h\upsilon - E_g) \quad (3)$$

Where ? is the absorption coefficient, h? is photon energy, B is a constant associated with a tail state density. By doing the linear relationship between (?h?)$^{1/2}$ and h?, the x-intercept of the linear extrapolation are the optical band gap E_g. The E_g values are from 2.13 eV to 2 .64 eV and decreases monotonously, which far less than the band gap (4.5 eV) of Si_3N_4 [13]. The Si/N atom ratio is calculated close to 1.15 and the films show Si-rich states. Y.H.Wang etc's [14] research showed that larger optical band gaps were caused the quantum effect of nanoscale silicon quantum dots. However, the silicon cluster has larger volume and the quantum effect is not obvious, so the band gap values were lower.

Urbach energy E_U is the absorption edge of the tail band width caused by the degree of disorder of the films [15]. The E_U value can be used to analyze the relevant information of the degree of disorder of the film materials. Urbach energy E_U's formula is as follows [16]:

$$\alpha\ (h\upsilon) = \alpha_0 \exp[(h\upsilon - E_0)/E_U]. \quad (4)$$

Where α_0 is the absorption coefficient at the position of optical band tail, E_0 is photon energy. Fig.4 is the E_U value of the films prepared with different hot wire temperatures. From fig.4 we can know that the change trends of E_U are consistent with that of E_g. With increasing of the hot wire temperature, the degree of disorder of films increases, the degree of order decreases. The reason is that when the temperature of the hot wire is below 1600 ℃, in the films there are certain amounts of hydrogen. Due to the passivation effect of the hydrogen atoms, the films are more easily relaxation and order. When the temperature of the hot wire is higher than 1600 °C, the hydrogen atoms completely spills out of the films, and the suspension bonds increase, the degree of order of the films also decreases, and it also widen the absorption band tail.

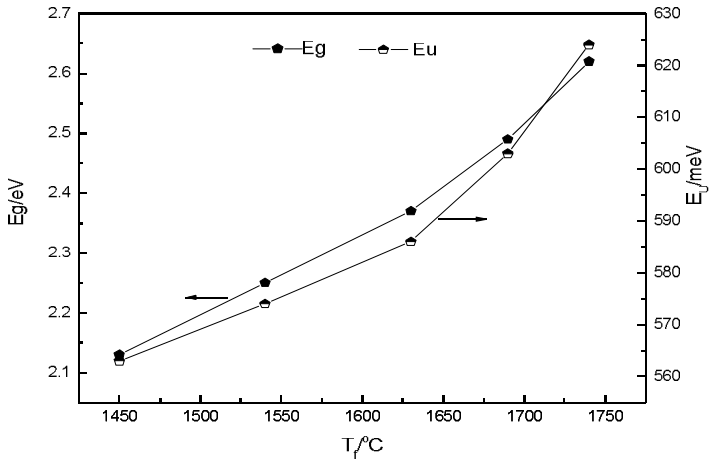

Fig. 4 The effects of different hot wire temperatures on E_g and E_U

3.3 PL spectra analysis

PL spectrum can be used to analyze the change of quantum dots in silicon nitride films [15]. The PL

spectra of all samples were measured at room temperature. There are a large number of defect states in the silicon nitride films prepared by the hot wire method, so the photoluminescence spectra are more complicated. It is generally believed that the photoluminescence of silicon nitride comes from the following two cases [17,18]. One is the radiation recombination of defect states in the forbidden band, such as N and Si atoms defects. The other is the quantum confinement effect luminescence caused by silicon quantum dots [19].

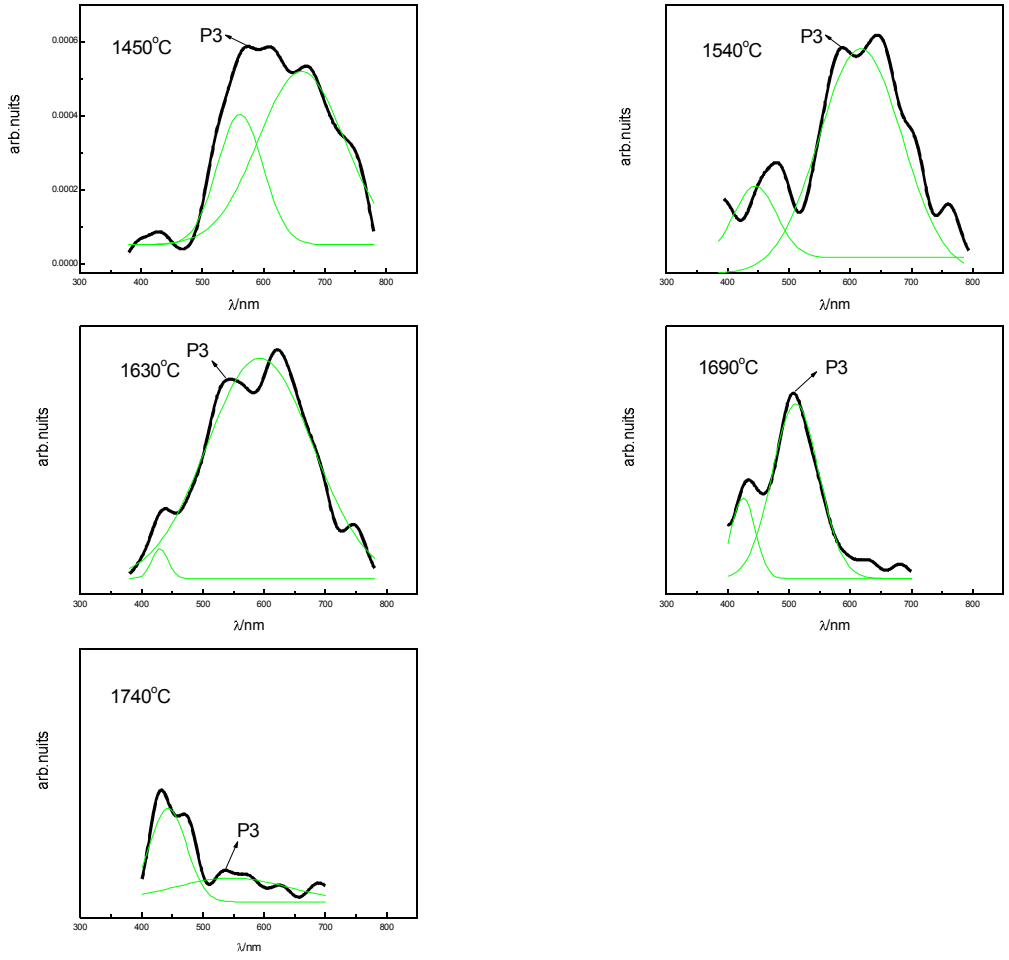

Fig.5 The change of P_3 peaks from room temperature PL spectra with different hot wire temperature

Figure 5 is the PL spectra of the films prepared at different hot wire temperatures. The samples were measured by the laser at the wavelength of 325nm of the Xenon lamp. The PL peaks are located at around 430nm (P1), 468nm (P2), 500-560nm (P3), and 645nm (P4), respectively. With the increase of the heat wire temperature, the shape and intensity of the PL luminescence peaks are changed. The researches show that the positions of the defect state PL peaks only are related to the defect state energy level, are not related to the others [20]. So the positions of the defect state PL peaks are not moving [21]. The wavelength of P_1, P_2, and P_4 peaks did not change with the changing of the hot wire temperature. Therefore, the P_1, P_2, and P_4 peaks are believed to be the defect state luminescence. For P_1 peak [22], it originates from the defect state luminescence of ≡Si0→ ≡Si-Si≡. The intensity of the P_1

peak firstly decreases and then increases. It is known from infrared analysis that, when the hot wire temperature of is below 1630℃,there are some H atoms in the films, and with the H passivation effect, the defect states in the samples are reduced. When the hot wire temperature is higher than 1630°C, the H atom spilled out of the films, and the suspension bonds have not been effectively passivated. At the same time, the increase of high-energy Si-N bonds leads to enhance the intensity of the P_1 peaks. The P_2 peak[23]is attributed to the luminescence of the electron Si-⟶ = N- defect state. With increasing of hot wire temperature, their luminous peaks gradually decreases to disappear. The P4 peaks at around 640nm are caused by the band tail state luminescence of silicon nitride samples [24].

Regarding the P3 peak, its peak position is between 504-572 nm (green light), which is consistent with the PL spectra peak's position (460-610nm) of Si quantum dots in silicon nitride films that usually observed [25, 26]. As the temperature of the hot wire increases, the P_3 peaks position have a significant red-shift phenomenon, so it can be attributed to the change of size and distribution of the Si QDs with the change of the hot wire temperature. Previous studies have found that[27,28], when the average size of the Si QDs becomes larger, the P_3 peaks produce a red-shift phenomenon (long wave direction movement). When the average size of the Si QDs becomes smaller, the P_3 peaks of the PL produce a blue-shift phenomenon (short wave direction movement).

Comparison of five figures in figure5, it can be seen that when the hot wire temperature is 1450°C, there are already a small amount of silicon nanoclusters in the films. When the temperature rises to 1540°C, the P_3 peak's position has a blue shift phenomenon and the P_3 peak intensity decreases. When the temperature of the hot wire rises from 1540°C to 1690°C, the P_3 peak's position has a red shift, and the peak intensity continues to weaken. When the hot wire temperature rises to 1740°C, the P_3 peak's position continues to red-shift, and the intensity decreases significantly. Among them, the P_3 peak intensity reaches a local maximum at the hot wire temperature of 1450°C. This is because H atoms in the films do not completely overflow the films, and H atoms play a role in passivation effect of the non-radiation recombination defect on the film surface. When the temperature of the hot wire reaches 1740°C, the H atoms in the films have completely overflowed, resulting in a local minimum of the P_3 peak intensity. This is consistent with the results of the FTIR analysis. Based on the above discussion of the changes of the peak position and intensity of the P_3 peak, it is shown that the photoluminescence peak in the range of 504-572 nm originates from the Si QDs.

IV. CONCLUSIONS

As the silicon nitride films were prepared by HWCVD, the hot wire temperature as an important experimental parameter has a significant effect. The results show that with increasing of the hot wire temperature, the fracture of Si-H bonds and N-H bonds cause the density of Si-H and N-H bonds to decrease and H atoms overflow the films. A large number of Si suspension bonds N suspension bonds cannot be passivated, which causes the Si-N bond to recombine again. The density of the Si-N bond in the films increases. The stability and compactness of the films are improved. The decrease of the content of H atoms leads to the decrease of H atoms desorption, the enhancement of the defect state density, the broadening of the band gap, the decrease of the order of the films, and the presence of a certain rich silicon state. The increase of the hot wire temperature can fully relax the silicon nitrogen atoms in the films, which can facilitate the orderly silicon nitrogen network, and Si-Si bonds are more closely between the silicon atoms to form more small silicon cluster particles directly. It generates nanoscale silicon quantum dots cluster directly. Therefore, the silicon quantum dot materials

embedded in the silicon nitride matrix are prepared by hot wire chemical vapor deposition with a higher hot wire temperature without further annealing.

[1] Yu W, Meng L H, Geng C L, etc, Structural properties of hydrogenated amorphous silicon nitride films deposited by facing targets sputtering, Chinese Science Bulletin. 55(18)(2010) 1799-1804.

[2] Wang Y, Shen D Z, Zhang J Y, etc, Influence of thermal annealing on the structural and optical properties of Si2 rich Sil icon nitride films, Chinese Journal of Liquid Crystals and Displays. 20(1)(2010) 18-21.

[3] Liu F Z, Scott W, Lynn G, etc, Amorphous silicon nitride deposited by hot-wire chemical vapor deposition. Appl. Phys, 96(5) (2004) 2973-2979.

[4] Meng xiangsen, Song chenlu, Yu jingsong, etc, Low temperature APCVD preparation silicon nitride film, Ceramic Journal. 20(3)(1999).

[5] Yu jingsong, Qian xiaoqian, Ma qingsong, etc, Study on preparation of oxynitrogen-glass thin film by SiH4-NH3-CO2 system of APCVD, Journal of Silicate. 27(3)(1999) 365-369.

[6] Lanford W A, Rand M J, The hydrogen content of plasma-deposited silicon nitride, J Appl Phys.49(1978) 2473-2477.

[7] Cong qiuzi, Polycrystalline Silicon two-dimensional X-ray diffraction, Beijing: Science Press (1997).

[8] Molinari M, Rinnert H, Vergnat M, Improvement of the photoluminescence properties in a-SiNx films by introduction of hydrogen, Appl Phys Lett. 79(2001) 2172-2174.

[9] Shen xuechu, Semiconductor optical properties, Beijing:Science Press,307.

[10] Li T, Jerzy K, Kong W, etc, Interference fringe-free transmission spectroscopy of amorphous thin films, J Appl Phys. 88(2000) 5764-5771.

[11] Panchal A K, Solanki C S, Post deposition annealing temperature effect on silicon quantum dots embedded in silicon nitride dielec-tric multilayer prepared by hot-wire chemical vapor deposition, Thin Solid Films. 517(2)(2009) 3488-3491.

[12] LV Mercaldo,PD Veneri,E Esposito,et al,PECVD in-situ growth of silicon quantum dots in silicon nitride from silane and nitrogen, Materials Science & Engineering B. s159–160(11)(2009) 77-79.

[13] Yao riying Yang deren, Study on Thermal Treatment Properties of Silicon Nitride Thin Films Sedimented by PECVD，Zhejiang University.2006.

[14] Chen fengxiang, Cui rongqiang ,Meng fanying, PECVD's blunt effect on Silicon, Acta Energiae Solaris Sinica. 24(3)(2003) 349-352.

[15] B. Karunagaran, S. J. Chung, S. Velumani et al, Effect of rapid thermal annealing on the properties of PECVD SiNx thin films, Materials Chemisstry and Physics. 106(2007) 130-133.

[16] Chapin D M,Fuller C S,Pearson G L,J.A New Silieon p-n Junetion Photocell for Converting Solar Radiationinto Eleetrieal Power, APPl.Phys.25(5)(1954) 676-677.

[17] Yu wei, Li Bin, Guo shaogang, etc, Effect of hydrogen dilution on the structure characteristics of the FTS deposition a-Si: H thin film, Acta Photonica Sinica. 41(3)(2012) 307-310.

[18] Park N M, Kim T S, Park S J, Band gap engineering of amorphous silicon quantum dots for light-emitting diodes, Appl Phys Lett. 78 (71)(2001) 2575.

[19] J. Robertson, Electronic-structure of silicon-nitride, J. Phys. C .63(1)(1979) 4753 .

[20] Wang M,Li D,Yuan Z,et al, Photoluminescence of Si-rich silicon nitride:Defect-related states and silicon nanoclusters, Appl Phys Lett. 90 (13)(2007) 131903.

[21] Hao H L, Wu L K, Shen W Z,et al, Origin of visible luminescence in hydrogenated amorphous silicon

nitride, Appl Phys Lett.91(2007) 201922-201922-3.

[22] Huang R, Chen K, Qian B,et al, Oxygen induced strong green light emission from low-temperature grown amorphous silicon nitride films,Appl Phys Lett. 89(22)(2006) 221120.

[23] Liu Y, Zhou Y, Shi W, et al, Study of photoluminescence spectra of Si-rich SiNx films,Materials Letters. 58(2004) 2397-2400.

[24] A Aydinli,A Serpengüzel,D Vardar,Solid State Communications, 98(4)(1996) 273-277.

[25] Molinari M, Rinnert H, Vergnat M, Evolution with the annealing treatments of the photoluminescence mechanisms in a-SiNx: H alloys prepared by reactive evaporation, J Appl Phys. 101 (12)(2007) 123532.

[26] LV Mercaldo,PD Veneri,E Esposito,et al, Structural and optical properties of silicon quantum dots in silicon nitride grown in situ by PECVD using different gas precursors, Materials Science & Engineering B. 159(11)(2009) 74-76.

[27] Park N M,Choi C J,Seong T Y,et al,Quantum confinement in amorphous silicon quantum dots embedded in silicon nitride, Phys Rev Lett. 86(7)(2001) 1355-1357.

[28] LV Mercaldo,PD Veneri,E Esposito,et al,PECVD in-situ growth of silicon quantum dots in silicon nitride from silane and nitrogen, Materials Science & Engineering B. 159–160(11)(2009) 77-79.